Reorganization of Snowfall beneath Cloud Top within the Comma Head Region of Two Extreme U.S. East Coast Winter Cyclones

ANDREW JANISZESKI,[a] ROBERT M. RAUBER,[a] BRIAN F. JEWETT,[a] AND TROY J. ZAREMBA[a]

[a] *Department of Atmospheric Sciences, University of Illinois Urbana–Champaign, Urbana, Illinois*

(Manuscript received 8 November 2023, in final form 13 May 2024, accepted 5 June 2024)

ABSTRACT: This paper examines ice particle reorganization by three-dimensional horizontal kinematic flows within the comma head regions of two U.S. East Coast winter storms and the effect of reorganization on particle concentrations within snowbands in each storm. In these simplified experiments, the kinematic flows are from the initialization of the HRRR model. Ice particles falling through the comma head were started from either 9-, 8-, or 7-km altitude, spaced every 200 m, and were transported north or northwest, arriving within the north or northwest half of the primary snowband in each storm. The greatest particle concentration enhancement within each band was a factor of 2.32–3.84 for the 16–17 December 2020 storm and 1.76–2.32 for the 29–30 January 2022 storm. Trajectory analyses for particles originating at 4 km on the southeast side of the comma head beneath the dry slot showed that this region supplied particles to the south side of the band with particle enhancements of factor of 1.36–2.08 for the 16–17 December 2020 storm and 1.04–2.16 for the 29–30 January 2022 storm. Snowfall within the bands had two source regions: 1) on the north/northwestern side, from ice particles falling from the comma head, and 2) on the southeastern side, from particles forming at or below 4-km altitude and transported northwestward by low-level flow off the Atlantic. While the findings give information on the source of particles in the bands, they do not definitively determine the cause of precipitation banding since other factors, such as large-scale ascent and embedded convection, also contribute to snow growth.

SIGNIFICANCE STATEMENT: Wintertime storms along the east coast of North America can produce heavy snowfall, high winds, coastal flooding, and cold temperatures, resulting in major economic impacts within the northeast U.S. urban corridor. The heaviest snowfall typically occurs within snowbands, elongated narrow regions identifiable by high reflectivity on radar. This paper examines the potential sources of the ice particles contributing to the snowbands and how the flow fields throughout the storm can contribute to enhanced particle concentrations within the bands.

KEYWORDS: Precipitation; Snowfall; Stratiform clouds; Winter/cool season

1. Introduction

Wintertime extratropical cyclones forming along the east coast of North America have major economic impacts on the northeast U.S. urban corridor. At the northern end, Boston, Massachusetts, averages one major (>25 cm, 10 in.) and three moderate (>10 cm, 4 in.) storms in a winter season, while Washington, D.C., at the southern end, averages one major event every 4–5 years and one moderate event each year (Kocin and Uccellini 2005). The heaviest snowfall and occasional blizzard conditions occur within the cyclones' comma head region, north and west of the low pressure center. The combined effects of heavy snowfall, high winds, coastal flooding, and cold temperatures often create hazardous conditions over a widespread region in a single storm (Kocin and Uccellini 2005; Griffin et al. 2014; Picca et al. 2014).

When viewing the comma head region of these storms with radar, two different perspectives on snowfall organization arise (Janiszeski et al. 2023). The first, evident from low-level scans and composites of the National Weather Service Weather Surveillance Radar-1988 Doppler (WSR-88D) network, is that the heaviest snowfall occurs within quasi-linear bands characterized by higher radar reflectivity. In more extreme events, a distinct primary band is often present, extending for hundreds of kilometers, and aligned with a low- to midtropospheric axis of frontogenesis (Nicosia and Grumm 1999; Novak et al. 2004, 2009, 2010; Stark et al. 2013; Kumjian and Lombardo 2017). In some cyclones, several bands are present. Multibanded precipitation may be related to the presence of gravity waves, irregularities in the frontal slope (Hobbs and Locatelli 1978), or elevated convection, although the specific causes of multibanded precipitation remain a subject of ongoing research (Schultz and Knox 2007; Ganetis et al. 2018; Leonardo and Colle 2024).

The second perspective, from vertically pointing radars, is that precipitation organizes as fall streaks originating at cloud top within cloud-top generating cells. Studies dating back to the 1950s have observed reflectivity fall streaks descending from these cells, sloping as they are sheared by the environmental winds, and often merging into stratiform radar echo

Denotes content that is immediately available upon publication as open access.

Janiszeski's current affiliation: Department of Civil and Environmental Engineering and Earth Sciences, University of Notre Dame, Notre Dame, Indiana.

Zaremba's current affiliation: Department of Atmospheric and Earth Sciences, University at Albany, Albany, New York.

Corresponding author: Andrew Janiszeski, ajanisz2@nd.edu

DOI: 10.1175/WAF-D-23-0184.1

© 2024 American Meteorological Society. This published article is licensed under the terms of the default AMS reuse license. For information regarding reuse of this content and general copyright information, consult the AMS Copyright Policy (www.ametsoc.org/PUBSReuseLicenses).

Brought to you by University of Alabama in Huntsville | Unauthenticated | Downloaded 08/23/24 03:02 PM UTC

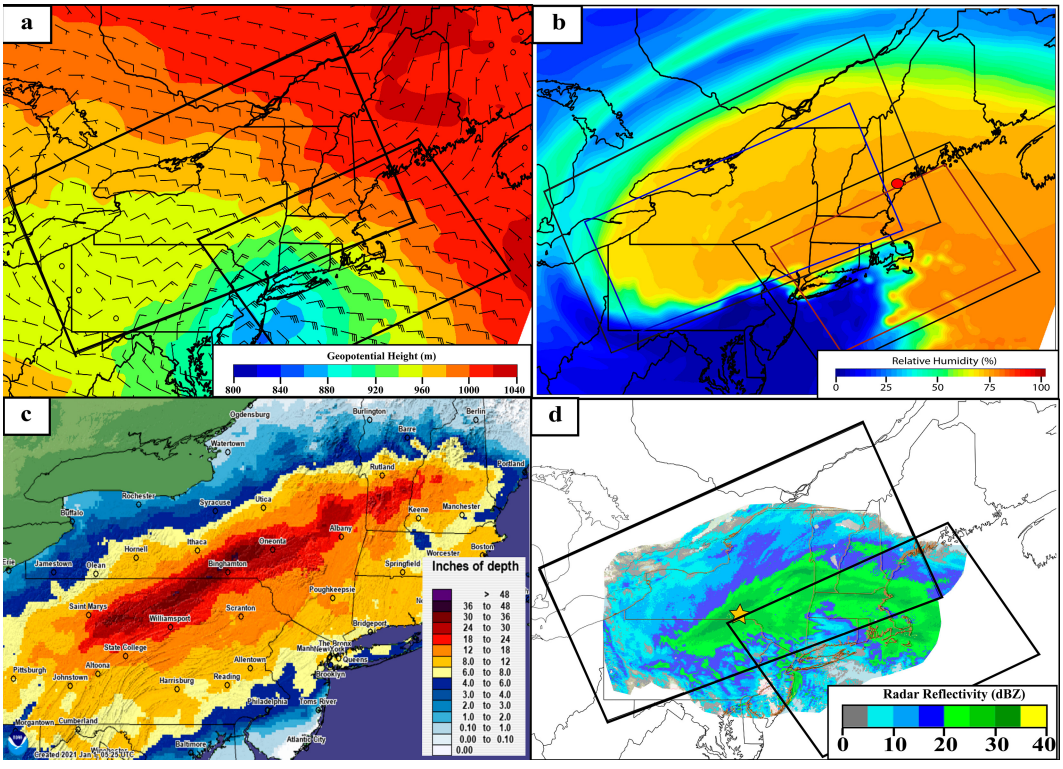

FIG. 1. (a) The 900-hPa geopotential height (m) and winds (m s^{-1}) from the HRRR model initialization at 0700 UTC 17 Dec 2020. The northern and southern KMDs are indicated by the black boxes; (b) 400-hPa HRRR model RH with initial particle release region for the northern (blue box) and southern (red box) KMDs (black boxes), and the location of 1200 UTC 17 Dec 2020 KGYX sounding (red dot); (c) 24-h snowfall (NOHRSC 2023) ending at 1200 UTC 17 Dec 2020; (d) WSR-88D MRMS composite of 2-km Z_e, Binghamton, NY (star), and KMDs (black boxes) at 0700 UTC 17 Dec 2020.

deeper within the clouds (Marshall 1953; Gunn et al. 1954; Wexler 1955; Douglas et al. 1957; Wexler and Atlas 1959; Carbone and Bohne 1975; Hobbs and Locatelli 1978; Syrett et al. 1995; Stark et al. 2013; Rosenow et al. 2014; Kumjian et al. 2014; Rauber et al. 2014, 2017; Plummer et al. 2014, 2015). Generating cells appear to be near-ubiquitous at cloud top within the stratiform regions of the comma head. The cells are typically 0.5–2 km wide, 1–2 km deep, with updrafts of 1–2 m s^{-1} (McFarquhar et al. 2011; Rosenow et al. 2014; Kumjian et al. 2014). Unfortunately, observations of generating cells are limited to two-dimensional time–height or spatial cross sections. To date, there are no measurements of the horizontal distribution of generating cells across the comma head, although idealized model simulations suggest that the cells organize differently in the horizontal depending on vertical wind shear within the cloud-top region (Keeler et al. 2017).

Because wintertime storms can produce heavy snowfall that can result in major economic impacts, forecasting the distribution of snowfall within these storms is important and requires an understanding of where snowbands are most likely to occur and what processes contribute to their formation. As stated in Janiszeski et al. (2023), snowbands occur as a result of any or all of three interrelated processes: 1) the concentration of ice particles into an elongated narrow region as a result of deformation and convergent flow, 2) the growth of particles within an elongated updraft as a result of the secondary circulation associated with frontogenesis, and 3) the growth of particles within convection triggered within updrafts associated with the secondary circulation. In general,

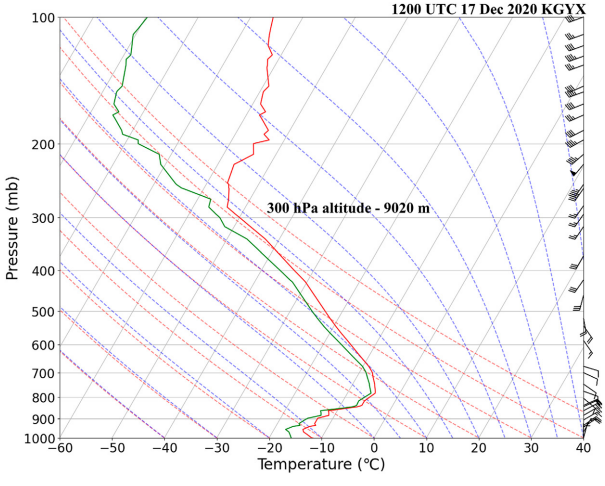

FIG. 2. Observed temperature, dewpoint temperature, and winds (long barb = 10 m s^{-1}) from the 1200 UTC 17 Dec 2020 KGYX sounding.

Brought to you by University of Alabama in Huntsville | Unauthenticated | Downloaded 08/23/24 03:02 PM UTC

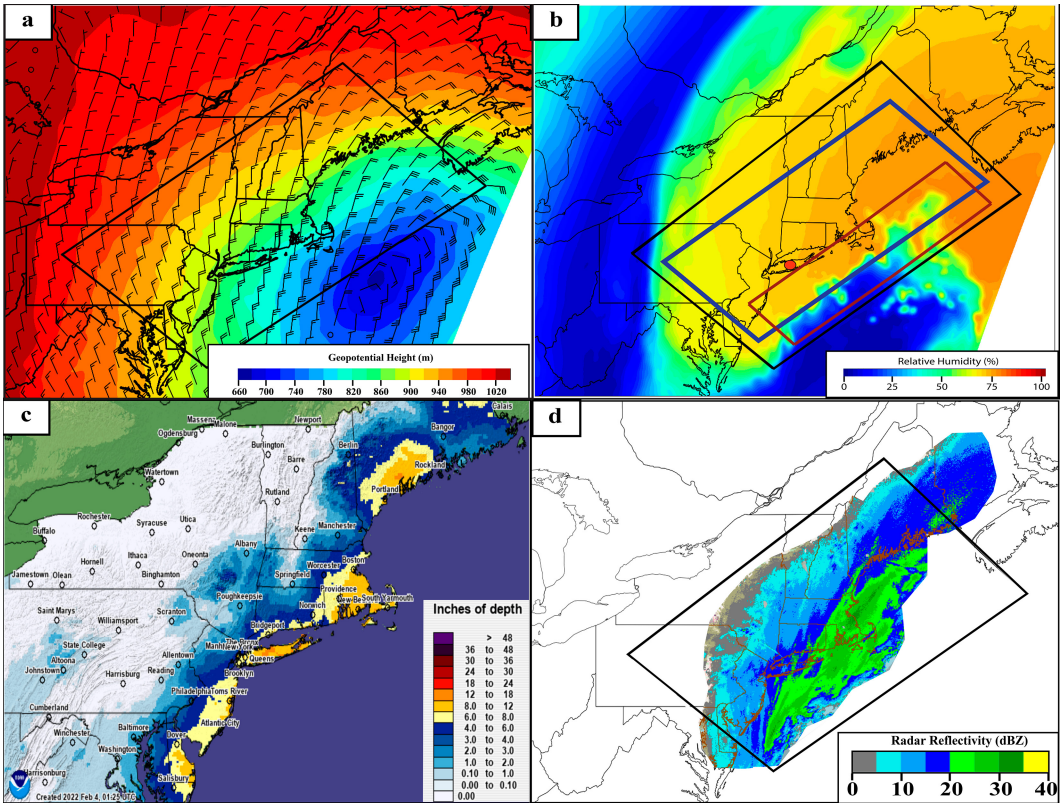

FIG. 3. (a) The 900-hPa geopotential height (m) and winds (m s^{-1}) from the HRRR model initialization at 1500 UTC 29 Jan 2022. The KMD is indicated by the black box; (b) 400-hPa HRRR model RH with initial upper-level particle release region (blue box) and lower-level particle release region (red box), both within the KMD (black box), and location of 1200 UTC 29 Jan 2022 KOKX sounding release (red dot); (c) 24-h snowfall (NOHRSC 2023) ending at 0000 UTC 30 Jan 2022; (d) WSR-88D MRMS composite of 2-km Z_e and KMD (black box) at 1500 UTC 29 Jan 2022.

convergence, frontogenesis, ascent, and relative humidity are correlated, and it can be difficult to disentangle the hydrometeor convergence signal from any of these factors. Janiszeski et al. (2023) attempted to bridge the two perspectives, focusing exclusively on the first process, divergent and convergent flow, by examining the reorganization of ice particles falling beneath cloud-top generating cells subject to two-dimensional convergence and stretching deformation kinematic flow fields. Their experiments with two-dimensional convergence showed that the enhancement of ice particle concentrations in the vicinity of low-level precipitation bands observed on radar occurred under conditions consistent with maximum particle residence time within the clouds, specifically when the cloud systems were deep and the particle fall speeds were slow. Their experiments with flow deformation showed that deformation provided little particle reorganization given typical deformation layer depths (1–4 km) and magnitudes (0.5–2.5 $\times$ 10^{-4} s^{-1}) within the comma head. They concluded that the primary cause of particle reorganization by flow kinematics was not by the deformation flow but rather through convergent flow across frontal zones.

This paper expands upon Janiszeski et al. (2023) by exploring how particles originating at cloud top across the comma head, falling with fall velocities characteristic of winter storms, are reorganized by the three-dimensional horizontal wind fields across the comma head and how localized increases in particle concentrations resulting from the horizontal wind contribute to the particle concentrations in the primary bands of two strong

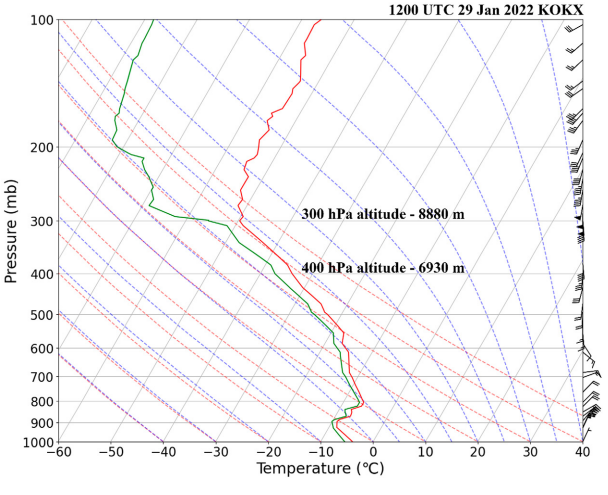

FIG. 4. Observed temperature, dewpoint temperature, and winds (long barb = 10 m s^{-1}) from the 1200 UTC 29 Jan 2022 KOKX sounding.

Brought to you by University of Alabama in Huntsville | Unauthenticated | Downloaded 08/23/24 03:02 PM UTC

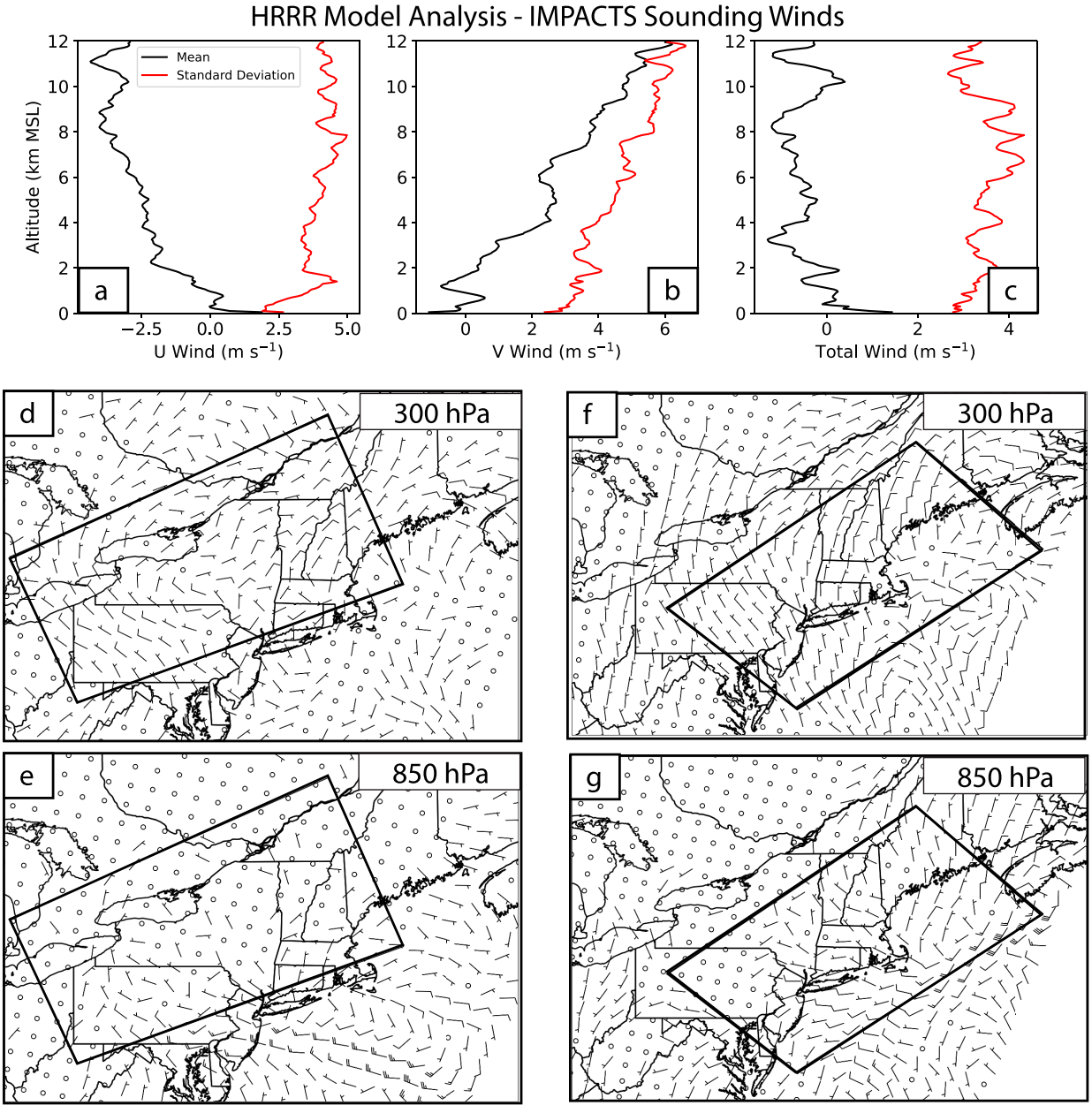

FIG. 5. Difference between HRRR model analysis sounding winds and observed winds from 75 soundings launched during the NASA IMPACTS field campaigns: (a) u component, (b) v component, and (c) total wind speed. (d) The 1-h change in HRRR initialization winds at 300 hPa between 0700 and 0800 UTC 17 Dec 2020. (e) The 2-h change in HRRR initialization winds at 850 hPa between 0700 and 0900 UTC 17 Dec 2020. (f) As in (d), but between 1500 and 1600 UTC 29 Jan 2022. (g) As in (e), but between 1500 and 1700 UTC 29 Jan 2022.

winter storms. These storms were selected because they were the two strongest cyclones along the East Coast occurring during the 2020–23 period of the National Aeronautics and Space Administration (NASA) Investigation of Microphysics and Precipitation for Atlantic Coast-Threatening Snowstorms (IMPACTS; McMurdie et al. 2022) field campaign. IMPACTS focused on understanding the physics and dynamics of banded precipitation, the dynamics and thermodynamics of cloud top and elevated convective substructures, and their relationship to microphysical processes within East Coast winter storms.

Section 2 provides a synoptic overview of each storm. Section 3 describes the kinematic model framework used to calculate the particle trajectories. Section 4 presents the results of the particle reorganization within each storm, while section 5 provides a discussion of the results in the context of previous measurements in cyclones. Section 6 summarizes the key findings of the study.

Brought to you by University of Alabama in Huntsville | Unauthenticated | Downloaded 08/23/24 03:02 PM UTC

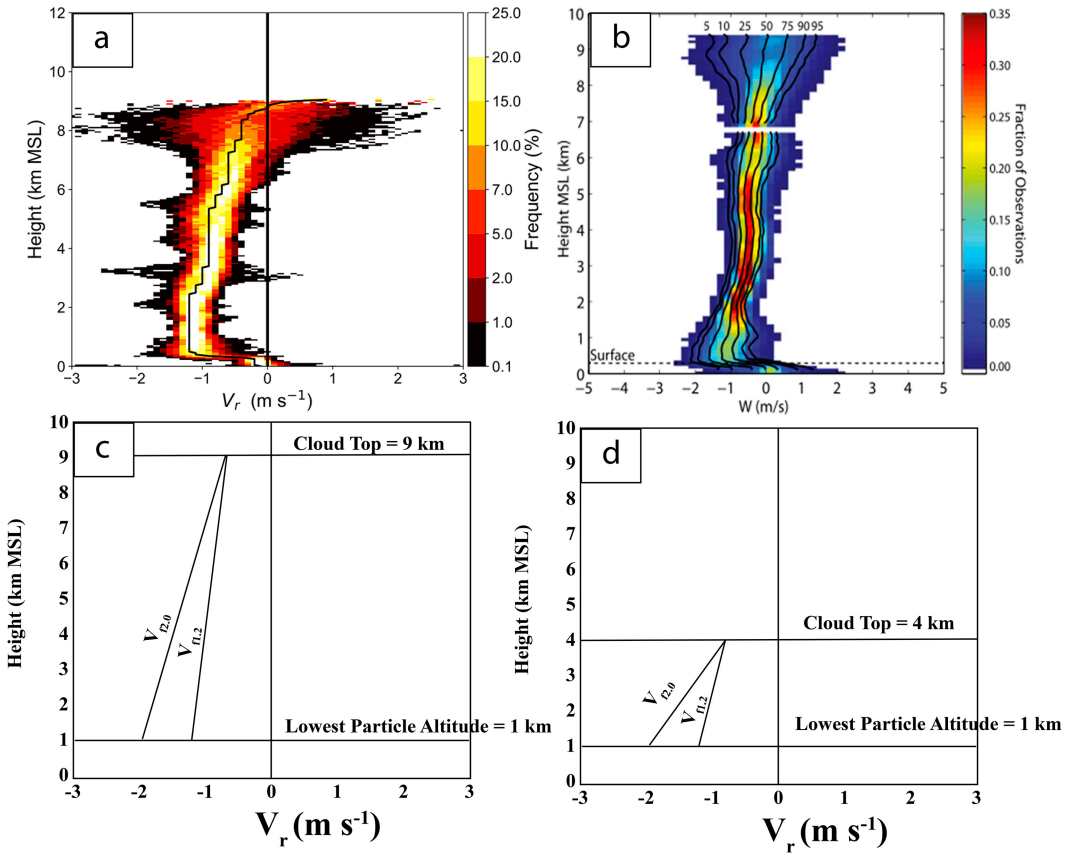

FIG. 6. (a) CFAD of vertical radial velocities measured by the CRS on the NASA ER-2 aircraft in the stratiform region of the comma head of a winter storm on 7 Feb 2020. The black contour shows the median vertical radial velocity values (from Varcie et al. 2023, their Fig. 8c). (b) As in (a), but for vertical radial velocities measured by the W-band University of Wyoming Cloud Radar on the National Center for Atmospheric Research C-130 aircraft in the stratiform region of the comma head of a winter storm on 8–9 Dec 2009. The black contours show the percent of observations with vertical radial velocities greater than the number noted on the contour. The median W contour most closely represents V_f of particles (from Rosenow et al. 2014, their Fig. 10). (c) Schematic of two ice particle fall velocity profiles used in the trajectory calculations with a cloud-top height of 9 km. (d) As in (c), but with a cloud-top height of 4 km.

2. Storm overview

The 16–17 December 2020 and 29–30 January 2022 storms were both high-impact cyclones with comma head regions characterized by deep stratiform clouds. The 16–17 December storm produced heavy snowfall over the interior Northeast United States, while the 29–30 January 2022 storm brought strong winds and heavy snowfall to coastal areas. Beneath the comma head region of both storms, moderate to heavy snow fell, particularly within a single large band of high radar reflectivity, as observed by WSR-88D radars.

a. The 16–17 December 2020 storm overview

The 16–17 December cyclone produced significant, and in some cases, record setting snowfall in portions of the interior Northeast United States. At 0700 UTC 17 December 2020, an area of low geopotential heights at 900 hPa was located along the southern New Jersey coast with a 20–30 m s^{-1} northeast wind along much of the East Coast from New Jersey northeastward to Massachusetts (Fig. 1a). The storm featured a deep comma head cloud structure over much of upstate New York and New England to the northwest of the 900-hPa low pressure center as seen in the 400-hPa relative humidity (RH) field from the 0700 UTC 17 December 2020 High-Resolution Rapid Refresh (HRRR) model initialization (Fig. 1b). To the southeast of the comma head, a dry slot with RH $<$ 25% extended across much of southeastern Pennsylvania eastward to central and southern New Jersey (Fig. 1b). Heavy snowfall accumulations occurred in locations impacted by the storm's major snowband, with a region of $>$61 cm (24 in.) extending northeastward from the north of State College, Pennsylvania, to Albany, New York, to the south of Rutland, Vermont (Fig. 1c). Locally, Binghamton, New York, and nearby locations received as much as 100 cm (40 in.) of snow in a 24-h period (Fig. 1c). The equivalent reflectivity factor Z_e from a Multi-Radar Multi-Sensor (MRMS; Smith et al. 2016) system WSR-88D radar composite at 2-km altitude at 0700 UTC 17 December 2020 shows a

Brought to you by University of Alabama in Huntsville | Unauthenticated | Downloaded 08/23/24 03:02 PM UTC

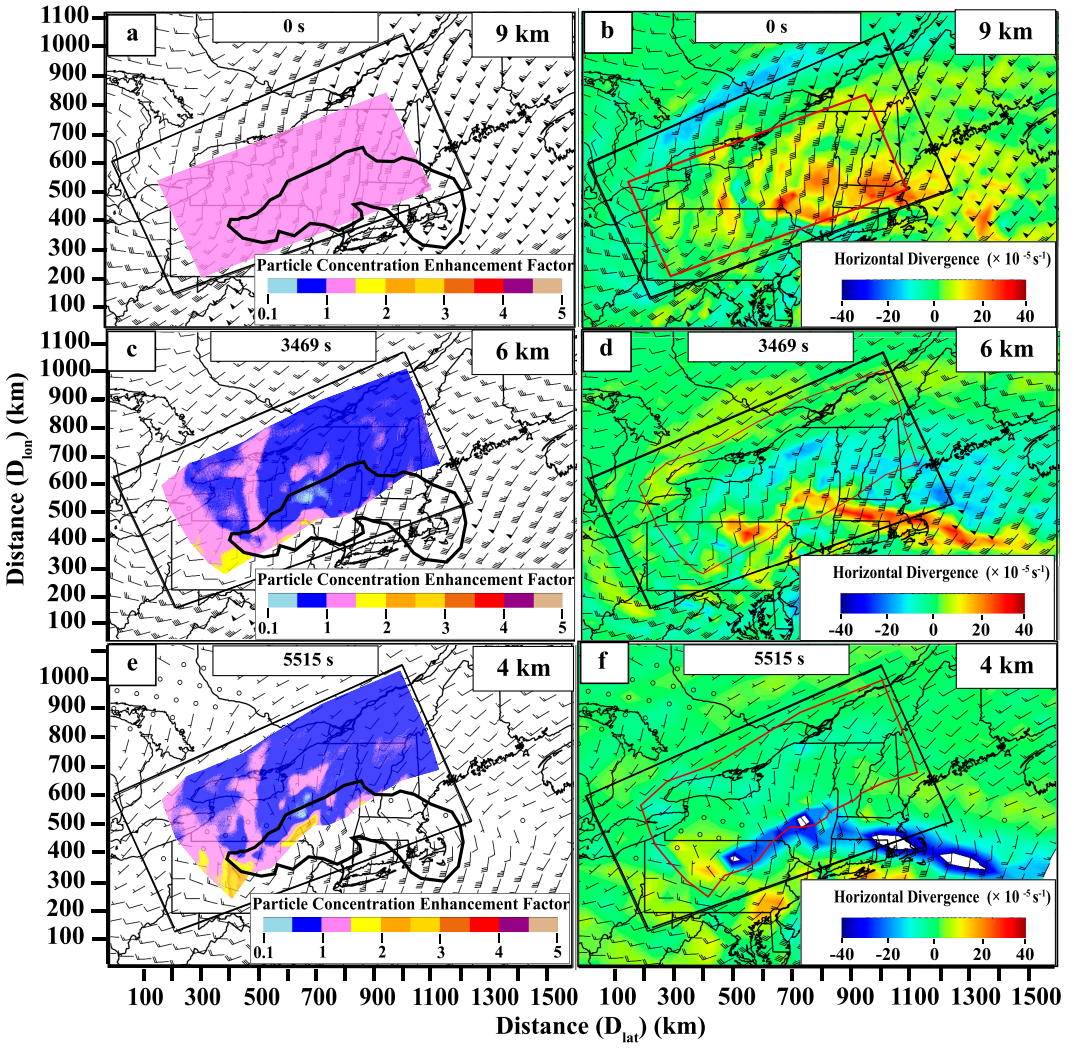

FIG. 7. Particle concentration enhancement factor E for control experiment and winds barbs at altitudes of (a) 9, (c) 6, and (e) 4 km; (b),(d),(f) horizontal divergence ($\times 10^{-5}$ s^{-1}) with v_h (m s^{-1}; long barb = 10 m s^{-1}) overlaid. The northern KMD is outlined in black on all panels, and the outline of particle distribution is shown in red in the rightmost panels. The 20-dBZ contour from the WSR-88D radars is shown in (a), (c), and (e) as a dark black line. The time since particle release is shown atop each panel.

well-defined band of heavy snowfall over the Binghamton, New York, area (yellow star) with Z_e = 30–35 dBZ_e. Further northeast, a swath of Z_e > 20 dBZ_e extended from eastern New York into southern Vermont, New Hampshire, and across northern Massachusetts (Fig. 1d).

Unfortunately, the 1200 UTC 17 December 2020 Albany, New York, sounding was unavailable. The 1200 UTC 17 December 2020 Gray, Maine (KGYX), sounding sampled the comma head of the storm characterizing the storm's cloud depth and wind structure (red dot, Fig. 2). The sounding showed the cloud top to be ~9.3 km. The HRRR model initialization, in close agreement with the sounding, indicated that the cloud top across the comma head was located at approximately 9 km. This storm featured a moderate south to southwesterly flow in the upper levels with a southerly flow of 30 m s^{-1} at 500 hPa veering to southwesterly and decreasing with height to 25 m s^{-1} at 300 hPa in the sounding. HRRR winds over the comma head in the same layer were similar, although the flow was stronger around 300 hPa with a south-southwesterly flow of 40–50 m s^{-1} found over much of the comma head region. Over the northwest portion of the comma head over Western New York, a weaker southerly flow of 10–20 m s^{-1} was found. Between 700 and 500 hPa, the KGYX sounding and HRRR model winds both had a southeasterly to south-southeasterly flow of 10–20 m s^{-1}. Between the surface and 800 hPa, the KGYX sounding winds, consistent with the HRRR model winds along the East Coast, were northeasterly between 10 and 20 m s^{-1}. Across the interior of New England and upstate New York, the northeasterly flow was weaker with winds between 5 and 10 m s^{-1}.

Brought to you by University of Alabama in Huntsville | Unauthenticated | Downloaded 08/23/24 03:02 PM UTC

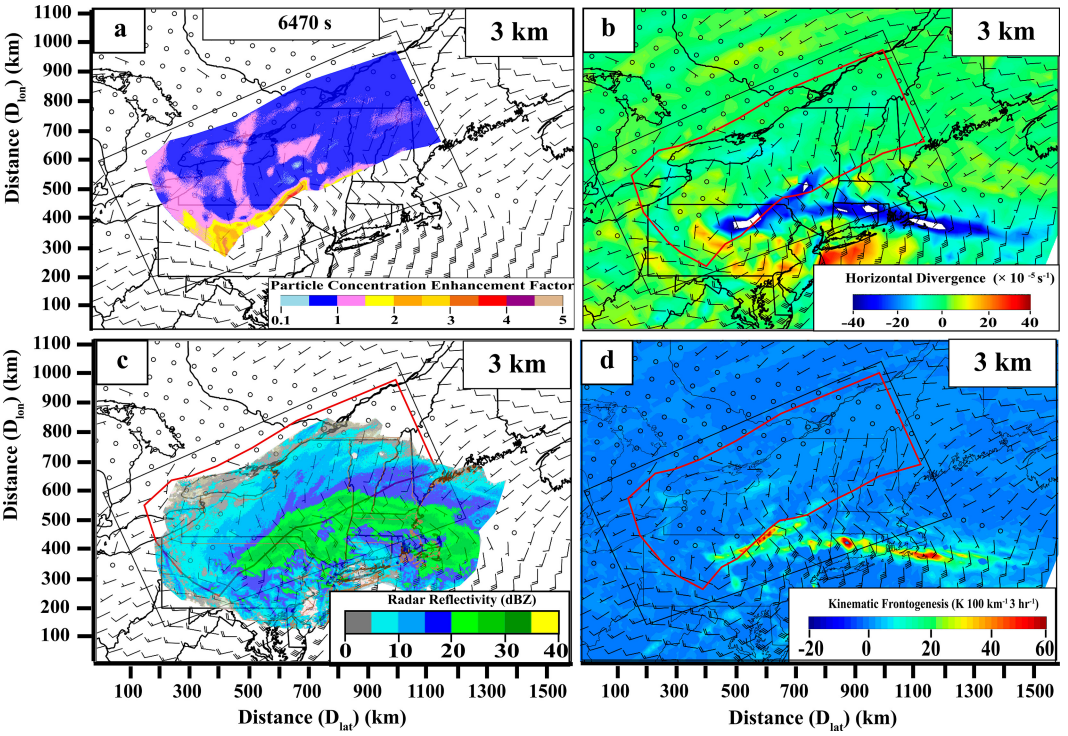

FIG. 8. The 3-km altitude winds (long barb = 10 m s^{-1}) together with (a) particle concentration enhancement factor E; (b) horizontal divergence ($\times 10^{-5} s^{-1}$) with outline of particle distribution (red); (c) WSR-88D MRMS Z_e composite at 3 km with particle distribution outline; and (d) frontogenesis [K $(100\ km)^{-1}$ $(3\ h)^{-1}$] with particle distribution outline. The time since particle release is shown atop (a).

b. The 29–30 January 2022 storm overview

The 29–30 January 2022 storm produced blizzard conditions along the northeast U.S. East Coast. The storm featured low geopotential heights at 900 hPa over the Atlantic Ocean east of Long Island and coastal New Jersey with a strong northerly flow of 30–35 m s^{-1} over coastal Massachusetts and adjacent areas (Fig. 3a). A distinct comma head, evident in the 400-hPa RH field from the HRRR model initialization at 1500 UTC 29 January 2022, extended from New Jersey and eastern New York into New England. A dry slot extended from just east of Cape Cod southward over the Atlantic Ocean (Fig. 3b). Twenty-four-hour snowfall reports ending at 0000 UTC 30 January 2022 from this storm showed that the heaviest snowfall (20–30 cm, 8–12 in.), with locally higher amounts, occurred across eastern Massachusetts, southeastern coastal Maine, and much of Long Island and Delaware, with much lighter snowfall inland of these coastal regions (Fig. 3c). At 1500 UTC 29 January 2022, a band of $Z_e > 20$ dBZ_e at 2 km MSL extended from the Gulf of Maine south-southwestward across southeastern Massachusetts, over the eastern tip of Long Island, and just offshore of the New Jersey coastline (Fig. 3d), coincident with the heaviest snowfall region.

The 1200 UTC 29 January 2022 Upton, New York (KOKX), sounding sampled the comma head region of the storm near the primary band (red dot, Fig. 4). This storm featured strong southerly winds in the upper troposphere, increasing with height from 20 to 50 m s^{-1} between 500 and 300 hPa. HRRR model winds in this same layer at 1500 UTC 29 January 2022 were similar across the comma head with a more southeasterly flow over the western side. The KOKX sounding shows a southeast to southerly flow of 10–20 m s^{-1} between 650 and 500 hPa which was consistent with HRRR model winds across the comma head in this region. Between 925 and 700 hPa, a strong northeasterly flow decreased with height from 35 to 20 m s^{-1}. HRRR model winds in the same layer were similar along the East Coast but were weaker and more northerly at 10–25 m s^{-1} across interior New England.

3. Kinematic framework

a. The 16–17 December 2020 storm KMDs

Particles arriving at low levels (1–3 km MSL) in the precipitation band in the 16–17 December 2020 storm had two possible source regions: the first within the deeper clouds with ~9-km tops northwest of the low pressure center and the second from shallower clouds with ~4-km tops beneath the intruding upper-tropospheric dry slot air. Two kinematic model domains (KMDs) were used (Fig. 1). These partially overlapped because the deeper high-level clouds partially overlapped the lower-level clouds beneath the dry slot (see Fig. 14, section 4). The northern domain with a 10-km top and the southern domain with a 4-km top were used to calculate the particle trajectories.

Brought to you by University of Alabama in Huntsville | Unauthenticated | Downloaded 08/23/24 03:02 PM UTC

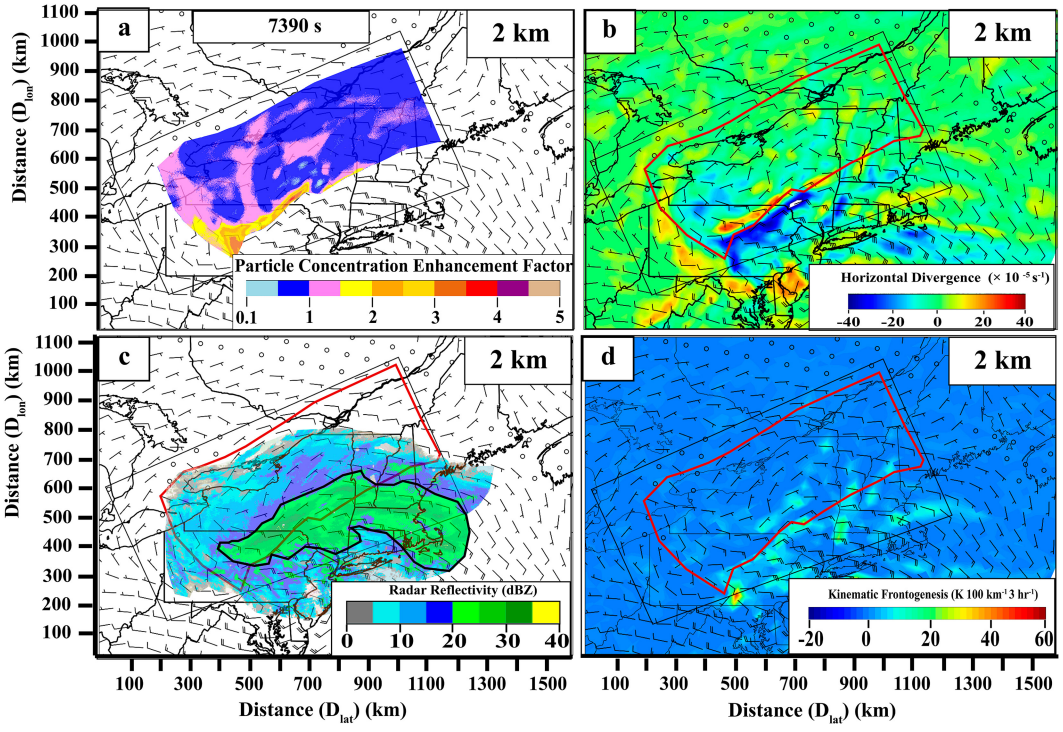

FIG. 9. As in Figs. 8a–d, but for 2-km altitude.

The northern KMD, based on HRRR model coordinates, was a quadrilateral grid that spanned 1033 km along its southeastern edge, 512 km along its southwestern edge, 569 km along its northeastern edge, and 962 km along its northwestern edge (Fig. 1b). This grid was designed to closely match the comma head of the storm at 400 hPa. For particle transport calculations, the kinematic model uses the full horizontal component of the winds from the HRRR model within the northern black box in Fig. 1b, interpolated to a cartesian grid where the x axis is parallel to the southern boundary, the y axis is parallel to the western boundary, and the vertical axis z is positive upward. The horizontal grid spacing in the northern KMD was 3 km, while the vertical grid spacing was 500 m, with a maximum altitude of 10 km, which was above the cloud top. Within the northern blue box in Fig. 1b, seven million particles were spaced every 200 m in x and y. These particles were initiated at one altitude in each experiment (Fig. 1b). This distribution resulted in particles spanning across the comma head region near the cloud top. The blue box was positioned toward the southeastern bound of the northern KMD such that the southeasternmost particles were located 20 km northwest of the southeastern edge of the northern KMD. This initial release positioning allowed particles to better fit the southeastern edge of the comma head cloud and allowed for advection to the northwest in the large-scale upper-tropospheric flow field (discussed in the next section), while keeping the particles within the northern KMD. The 200-m horizontal spacing of particles was sufficient to elucidate the impacts of the large-scale horizontal flow in reorganizing particles falling beneath the comma head. Due to the absence of three-dimensional cloud-top observations, the initial particle placement does not try to mimic enhanced concentrations of particles, as might be found with cloud-top generating cells (Keeler et al. 2017) but rather examines the trajectories of particles spread initially uniformly across the comma head near cloud top. The initial particle altitudes z_i of 9, 8, and 7 km were chosen based on both the HRRR model RH and 1200 UTC 17 December 2020 KGYX sounding analyses shown in section 2a.

The southern KMD was placed beneath the intruding dry slot air. The HRRR model RH fields in this region indicated that the cloud tops were ~4 km. The southern KMD spanned 675 km along its southern edge, 481 km along its western edge, 661 km along its northern edge, and 487 km along its eastern edge with the same horizontal and vertical grid spacing as the northern KMD. Within the red box in this domain, 5.25 million particles were spaced 200 m in x and y. All particles in the southern KMD were released at 4-km altitude.

b. *The 29–30 January 2022 storm*

For the 29–30 January 2022 storm, a single KMD was used. The KMD spanned 995 km along its southeastern edge, 579 km along with northeastern edge, 980 km along its northwestern edge, and 590 km along its southwestern edge (Fig. 3b). The grid spacing and particle spacing were the same as for 16–17 December 2020 storm. Based on the comma head cloud shape at 400 hPa and the large-scale flow, the particle release region (blue box) was placed with its southeastern

Brought to you by University of Alabama in Huntsville | Unauthenticated | Downloaded 08/23/24 03:02 PM UTC

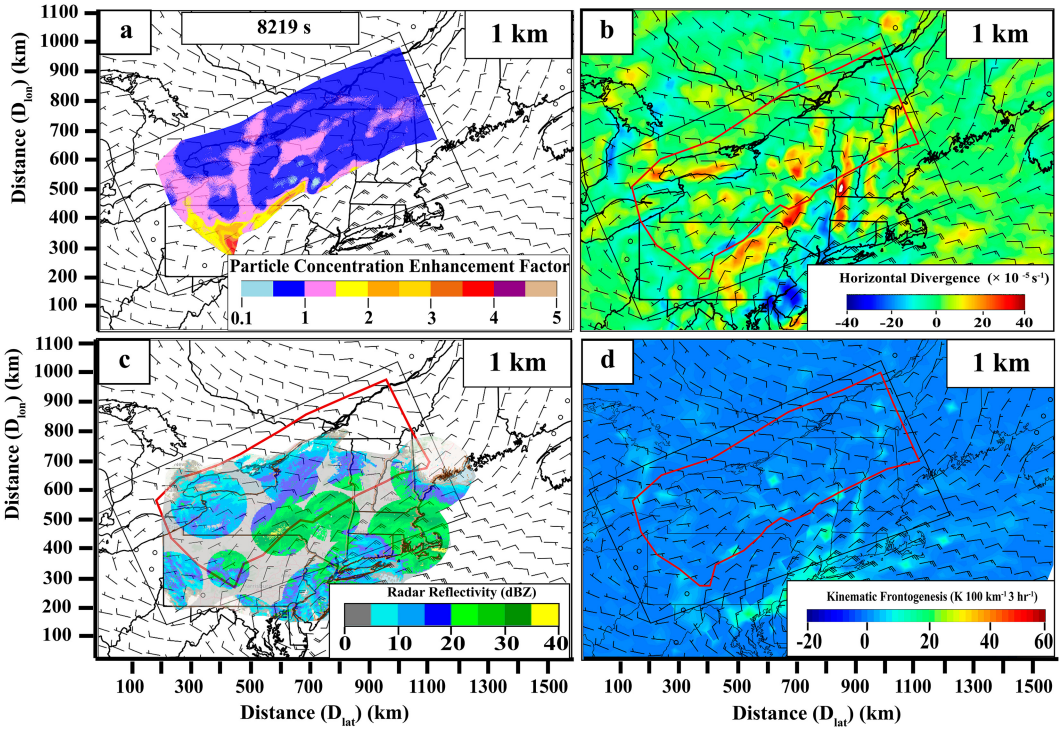

FIG. 10. As in Figs. 8a–d, but for 1-km altitude. Light gray regions in (c) were beneath the beam height of WSR-88D radars within the domain.

edge 100 km northwest of the southeastern boundary of the KMD (Fig. 3b). As was the case for the previous storm, seven million particles spaced 200 m apart in x and y were started at one altitude in Fig. 3b for each experiment. The initial particle altitudes z_i of 9, 8, and 7 km were chosen based on both the HRRR model RH analysis and the 1200 UTC 29 January 2022 KOKX sounding shown in section 2b. The particle release region for the 4-km deep clouds beneath the dry slot is noted by the red box in Fig. 4b. The southern particle release region contained 3.35 million particles spaced 200 m in x and y and released at 4-km altitude. As with the previous case, the upper-level comma head clouds partially overlapped the clouds below the dry slot, so the release altitudes for particles at 9 and 4 km partially overlapped (see Fig. 20; section 4).

c. *Representativeness of HRRR model initialization wind field*

For each storm, horizontal winds were obtained across the comma head region from the HRRR model initialization at an hour when the bands were distinct and the snowfall was heavy. The representativeness of the HRRR model winds for these calculations was examined by comparing HRRR model initialization winds to 75 soundings launched during several different storms during the NASA IMPACTS campaign. The HRRR model winds used for the comparison were at the time and location of each sounding launch. The mean difference (HRRR − sounding) of the west–east u wind component increased from ~0 to ~−3 m s^{-1} between the surface and 10 km (Fig. 5a), the mean difference of the south–north v component increased from ~0 to ~5 m s^{-1} between the surface and 10 km (Fig. 5b), and the total wind speed difference varied between 0 and −1.5 m s^{-1} between the surface and 10 km, with a standard deviation of ~4 m s^{-1} in the total wind speed difference (Fig. 5c). In the specific cases of the trajectories simulated here, this potential variability cannot be accounted for since we have no true wind field to use as a substitute for the HRRR model initialization field. The wind field for the trajectory calculations was assumed to be invariant over the 2 h that the particles fell from 9 to 1 km MSL. In the first hour, the particles were subject to the upper-tropospheric flow, while in the second hour, particles fell through the lower troposphere. Figures 5d and 5f show the 1-h change in the 300-hPa HRRR model winds during the time the particles fell through the upper troposphere. The change in the model winds was on the order of 5 m s^{-1} or less for each storm. In the lower troposphere, the 2-h change in the HRRR model winds was 5 m s^{-1} or less across most of both domains (Figs. 5e,g). The continuous gradual change in the winds over the ~2-h period of particle descent assuming that a 5 m s^{-1} change in the upper and lower troposphere over 1 and 2 h, respectively, could lead to an approximate particle displacement error of ~18 km. Based on the wind difference in Figs. 5d–g, the displacement would likely be toward the south which would move particles toward the band in each storm.

d. *Particle fall velocity*

Ice particles were assumed to fall through a stratiform cloud with one of two ice particle fall velocity profiles. In

Brought to you by University of Alabama in Huntsville | Unauthenticated | Downloaded 08/23/24 03:02 PM UTC

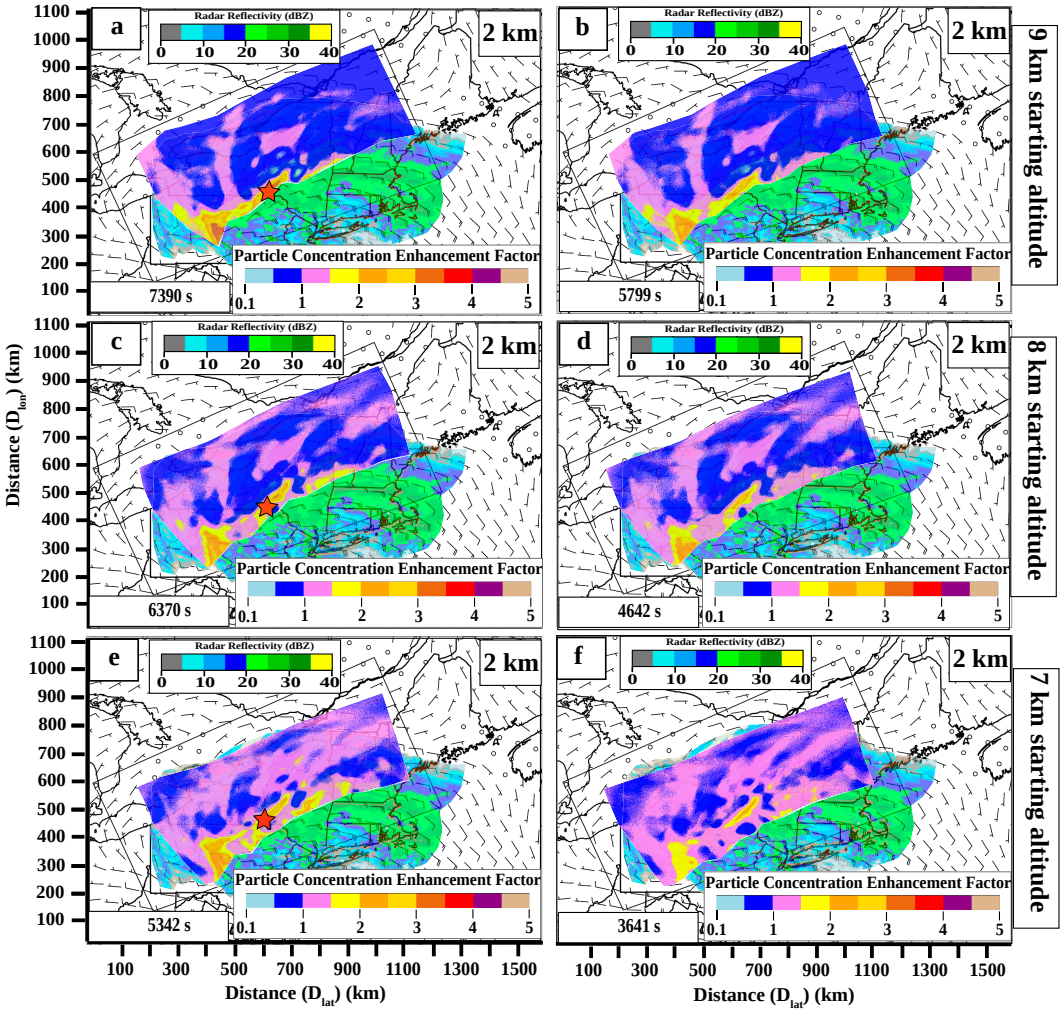

FIG. 11. Particle concentration enhancement factor E overlaid on the WSR-88D MRMS composite of Z_e, and v_h at 2 km for experiments with (a),(b) $z_i = 9$, (c),(d) $z_i = 8$, and (e),(f) $z_i = 7$ km. Panels (a), (c), and (e) use $V_{f,1.2}$, while panels (b), (d), and (f) use $V_{f,2.0}$. The time since particle release is shown in the bottom left of each panel.

one set of experiments, the ice particle fall velocity $V_{f,1.2}$ in each experiment varied from -0.8 m s^{-1} at cloud top to -1.2 m s^{-1} at 1-km altitude and was based on the contour frequency by altitude diagram (CFAD) analysis of the median vertical radial velocity of falling ice particles observed in the comma head region of midlatitude winter storms with airborne W-band radars during the IMPACTS and Profiling of Winter Storms (PLOWS) projects (Figs. 6a,b). Previous work in Griffin et al. (2014), Picca et al. (2014), and Ganetis and Colle (2015) documents the presence of large, rimed snow aggregates in some storms. To account for this, another set of experiments had fall velocities vary from -0.8 m s^{-1} at cloud top to -2.0 m s^{-1} at 1-km altitude ($V_{f,2.0}$) to parameterize the effects of snow growth, resulting in large, rimed snow aggregates (Locatelli and Hobbs 1974). Figures 6c and 6d show these two fall velocity profiles between cloud top at 9-km (northern particle release region; Figs. 1 and 3) or 4-km (southern particle release region; Figs. 1 and 3), and 1-km altitude, the approximate height where the particles would be observed by ground-based radars.

e. *Particle trajectories*

For horizontal and vertical particle motion, a two-step bilinear interpolation scheme, similar to that of Draxler and Hess (1998) was used. In the first step, the scheme calculated an estimated particle final position (x_e, y_e) based on the wind components at the particle initial position (x_i, y_i). For the next step, the wind components midway between (x_i, y_i) and (x_e, y_e) were determined and used to calculate the actual particle final position (x_f, y_f). In 1 s, particles fell at the assigned V_f and were transported by the horizontal wind. The process was then repeated until the particles descended to a 1-km altitude.

The two storms both exhibited deep stratiform clouds. The control experiment for the northern release regions in these storms used a starting altitude $z_i = 9$ km and $V_{f,1.2}$. Particle distributions together with convergent and divergent

Brought to you by University of Alabama in Huntsville | Unauthenticated | Downloaded 08/23/24 03:02 PM UTC

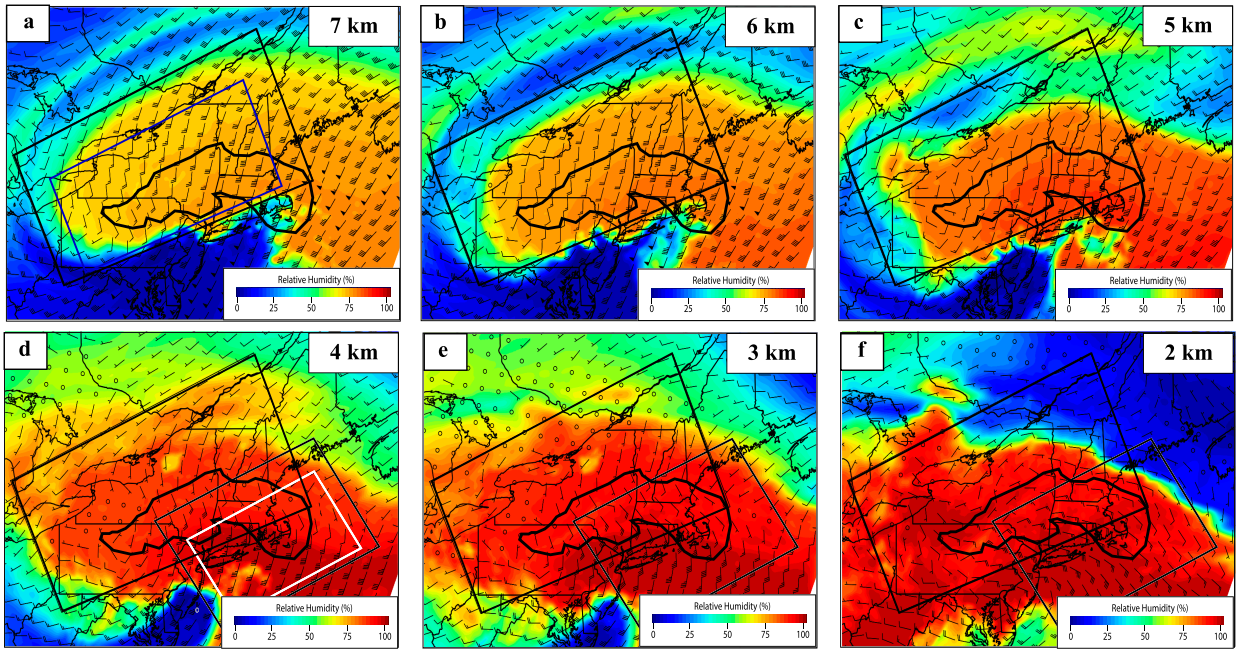

FIG. 12. HRRR model RH from the 0700 UTC 17 Dec 2020 HRRR initialization overlaid on υ_h at (a) 7-, (b) 6-, (c) 5-, (d) 4-, (e) 3-, and (f) 2-km altitude. The edge of 2-km Z_e 20 dBZ_e is shown by the black outline in all panels. Winds are expressed in meters per second with long barb = 10 m s^{-1}. The KMD for the comma head region is shown in all panels, while the KMD for the southeast sector in (d), (e), and (f). The particles were initialized within the blue box in (a) in the comma head region and the white box in (d) for the southeast region.

flow fields were examined every 1 km between 9- and 4-km altitude. Then, particle concentration enhancements were compared with Z_e, convergent/divergent flow regions, and frontogenesis at 3-, 2-, and 1-km altitudes. Sensitivity experiments were then carried out comparing $V_{f,1.2}$ and $V_{f,2.0}$ with particle release altitudes of z_i of 9, 8, and 7 km in the northern particle release regions. In the southern release regions, particles were released at one altitude, 4 km, using each of the fall velocity profiles.

4. Particle reorganization by three-dimensional horizontal winds

The purpose of this research is to determine how the three-dimensional horizontal flow υ_h reorganizes falling ice particles initially uniformly spread at cloud-top altitudes within both the comma head region and the region below the upper-tropospheric dry slot, and whether particle concentrations are enhanced in the vicinity of the primary low-level band within each storm. To demonstrate this, the ice particle concentration enhancement factor E was calculated at every 1-km altitude below z_i and related to the HRRR model horizontal flow. The quantity E was calculated by taking the number of particles in 1-km^2 horizontal bins at every analysis altitude and dividing that by the number of particles in the same bin in the uniform distribution at z_i. A value of E less than 1 signifies a decrease in the particle concentration in a bin, while values greater than 1 signify an increase in the particle concentration in the bin. At lower altitudes, E is examined in the context of the flow, regions of convergence/divergence and frontogenesis, and WSR-88D observed radar reflectivity.

a. *The 16–17 December 2020 storm analysis*

1) CONTROL EXPERIMENT (NORTHERN KMD)

Figures 7a–f display the ice particle reorganization at 9, 6, and 4 km for the control experiment for the northern KMD, which had z_i = 9 km with a $V_{f,1.2}$ profile. Positions (D_{lat}, D_{lon}) are referenced in kilometers with respect to the larger HRRR model grid with the origin at 37°N, 83°W (Fig. 7). The term "domain," as used here, refers to the northern KMD within the black box in Fig. 7.

In general, the particles over the northeast portion of the domain (D_{lat} = 700–1000 km, D_{lon} = 550–1000 km) falling from 9- to 4-km altitude were subject to a southerly to south-southwesterly flow that decreased with decreasing altitude from 50 to 10 m s^{-1} (Figs. 7b–f). Over the western portion of the domain between D_{lat} = 100–400 km, υ_h was much weaker with westerly flow curving cyclonically to a southerly flow, with magnitudes of 5–10 m s^{-1} between 9- and 6-km altitudes, and even weaker westerly or, in some locations, calm winds between 6- and 4-km altitudes. The location and magnitude of particle reorganization can be understood in terms of the winds and horizontal divergent and convergent flow regions (Figs. 7b,d,f). Regions of horizontal flow with divergence values of 25–40 $\times$ 10^{-5} s^{-1} were located within the southeastern portion of the domain between 9- and 7-km altitude (D_{lat} = 500–100 km, D_{lon} = 400–550 km) (Figs. 7b–d). The values of

Brought to you by University of Alabama in Huntsville | Unauthenticated | Downloaded 08/23/24 03:02 PM UTC

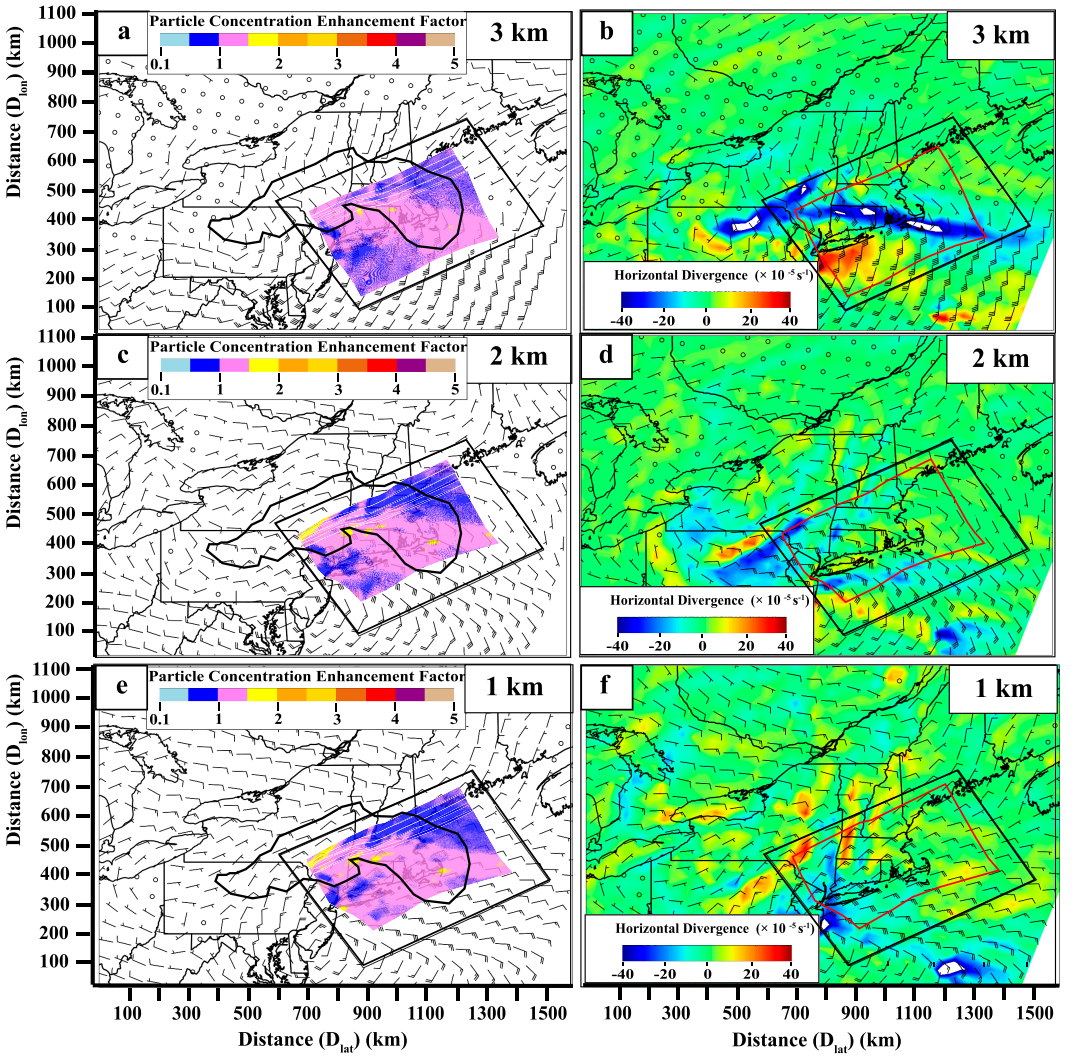

FIG. 13. Particle concentration enhancement factor E for the southeast region for the control experiment and winds barbs at altitudes of (a) 3, (c) 2, and (e) 1 km; (b),(d),(f) horizontal divergence ($\times 10^{-5}$ s^{-1}) with v_h (m s^{-1}; long barb = 10 m s^{-1}) overlaid. The KMD for the southeast region is outlined in black on all panels, and the outline of the particle distribution is shown in red in the rightmost panels. The 20-dBZ contour from the WSR-88D radars is shown in (a), (c), and (e) as a dark black line.

E ranged from 0.84 to 0.96 across this region at 8 and 7 km (not shown), indicating that divergent flow was decreasing particle concentrations below their original value at z_i. Between 5 and 4 km (Fig. 7e), a narrower elongated region of convergence occurred (D_{lat} = 550–1100 km, D_{lon} = 400–550 km) with divergence values between -20×10^{-5} and -40×10^{-5} s^{-1} (Fig. 7f). As a result, E increased in a narrow band-like shape stretching from southwest to northeast, to values of 1.84–2.96 between D_{lat} = 550–700 km and D_{lon} = 400–550 km, with the greatest E of 2.36–2.96 between D_{lat} = 630–680 km and D_{lon} = 470–500 km (Fig. 7e). Another region of E = 1.76–2.92 was centered at D_{lat} = 400 km between D_{lon} = 250 and 300 km (Fig. 7e). This may have resulted from the localized area of cyclonic flow curvature at 4–5 km in that region.

Figures 8a–d examine E in the context of horizontal divergence, frontogenesis, and radar reflectivity at 3-km altitude. The red outline in Figs. 8b–d indicates the outside edge of the ice particle distribution. In Fig. 8a, the greatest particle concentration increase, E= 2.32–3.84, is located slantwise from southwest to northeast at the southeastern edge of the distribution bounded by D_{lat} = 300–680 km, D_{lon} = 300–530 km. This region is collocated with the northwest side of a zone of convergent flow with horizontal divergence values from -18 to -40×10^{-5} s^{-1} and southeast winds that range from 5 to 15 m s^{-1} (Fig. 8b). The northwest side of the main snowband is located in the same region, with Z_e ranging between 25 and 30 dBZ_e (Fig. 8c). Exceptionally strong localized values of frontogenesis of 30–55 K (100 km)$^{-1}$ (3 h)$^{-1}$ are also found in this region (Fig. 8d). On the southwest edge of this region, a

Brought to you by University of Alabama in Huntsville | Unauthenticated | Downloaded 08/23/24 03:02 PM UTC

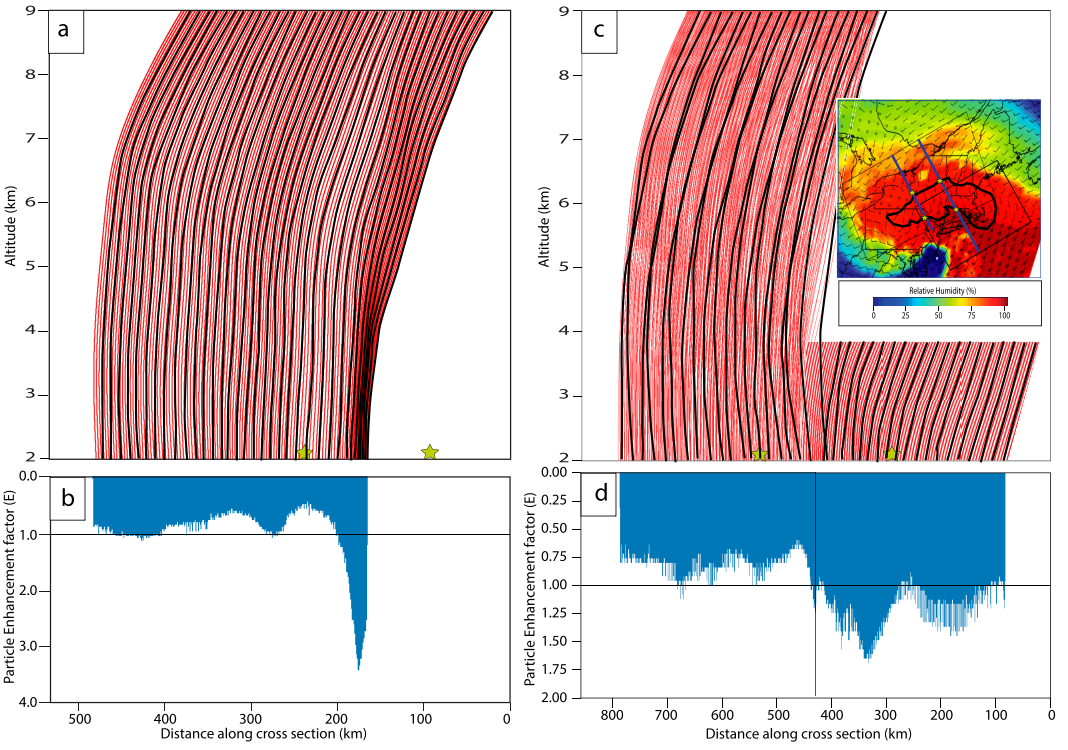

FIG. 14. (a) Red, full set of 2D trajectories of particles originating in the northern KMD and descending from 9 km in the cross-sectional plane along the western blue line in the inset in (c); black lines show the select trajectories. The stars denote the boundaries of the 20-dBZ contour in the inset. (b) Histogram of particle enhancement factor E corresponding to the trajectories in (a). (c) As in (a), except that the particles are descending along the eastern blue line in the inset from 9 km in the northern KMD and 4 km in the southern KMD. (d) Histogram of the particle enhancement factor E corresponding to the trajectories in (c). Inset: RH and wind at 4 km with both KMDs. The blue lines correspond to the cross sections in (a) and (c).

zone of E = 2.2–3.32 occurred (bounded by D_{lat} = 300–370 km, D_{lon} = 250–370 km) (Fig. 8a). This region was not collocated with higher values of convergence (Fig. 10b) or frontogenesis (Fig. 8d) and was likely associated with particle concentration increases associated with flows at higher altitude (see Fig. 7). The rest of the particle distribution had an E of 0.84–1.24 with a local minimum of 0.36 at approximately D_{lat} = 700 km and D_{lon} = 580 km. This region was found to the northwest of the heavier snowfall observed by radars, atop a broad and diffuse region of Z_e less than 15 dBZ_e (Fig. 8c). No ice particles from the comma head arrived within the southern half of the main precipitation band at 3 km. The source of particles in this region will be discussed later in this section.

Figures 9a–d show the same analysis as Figs. 8a–d except for 2-km altitude. The magnitude and location of E are similar to Fig. 8a. Subtle differences are noted in Fig. 9b near the southeast edge of the particle distribution when compared to Fig. 8b in that a narrow region of divergence of 20–25 $\times$ 10^{-5} s^{-1} appears just northwest of the convergent region, which had values from -30 to -40 $\times$ 10^{-5} s^{-1}. An east-northeast flow of 15–20 m s^{-1} and pockets of frontogenesis with values of 15–20 K $(100\ \text{km})^{-1}$ $(3\ \text{h})^{-1}$ was spaced throughout the southeastern portion of the domain (Fig. 9d). Again, most of the particle enhancement region lies within the northern portion of the snowband (Fig. 9c). As with 3 km, at 2-km altitude, no ice particles from the comma head were located in the southern half of the band (Fig. 9c).

Figures 10a–d show the same analyses as Figs. 8a–d except for 1-km altitude. The MRMS radar coverage at this altitude was poor (Fig. 10c). The distribution of E again is similar to Figs. 8a and 9a with subtle differences. In Fig. 10a, a band of concentration enhancement of 2.28–3.68 was found extending from southwest to northeast over a region bounded by D_{lat} = 550–680 km, D_{lon} = 400–530 km. This was a 0.04–0.16 decrease in E compared with Figs. 8a and 9a for that region. Additionally, another maximum in E = 3.12–4.36 was found at the southwest corner of the distribution near D_{lat} = 320 km; D_{lon} = 250 km. This was an increase of 0.92–1.04 in that region compared to 3- and 2-km altitude. Figure 10b shows the divergence of 20–25 $\times$ 10^{-5} s^{-1} located just southeast of the particle distribution (red line) in a 15–20 m s^{-1} northeasterly flow with a few pockets of weak divergent flow found elsewhere in the KMD. Figure 10c, similar to Fig. 9c, shows that the maximum Z_e values within the northern part of the precipitation band were collocated with the southwest to northeast band of larger E values, while the rest of the distribution was coincident with much weaker Z_e to the northwest of the band. Figure 10d shows only isolated pockets of the frontogenesis of

Brought to you by University of Alabama in Huntsville | Unauthenticated | Downloaded 08/23/24 03:02 PM UTC

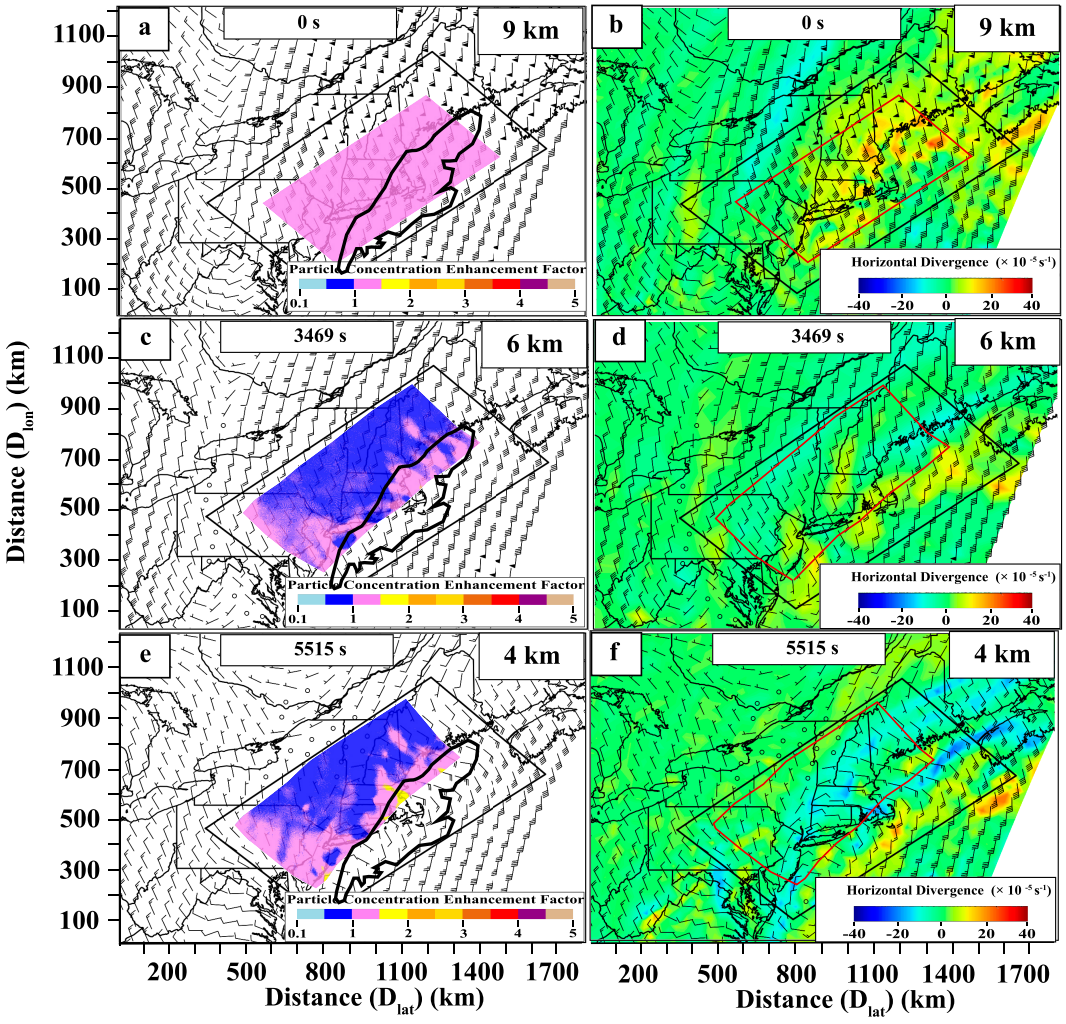

FIG. 15. As in Figs. 7a–f, but for the 29–30 Jan 2022 storm.

approximately 10 K $(100\ \text{km})^{-1}$ $(3\ \text{h})^{-1}$ mainly over the southeast portion of the KMD.

2) SENSITIVITY STUDIES (NORTHERN KMD)

At 1-km altitude, radar coverage was incomplete to capture banded precipitation. To relate reflectivity to E, the 2-km altitude MRMS reflectivity composite was used on which to overlay E to illustrate the sensitivity of particle reorganization to both z_i and the two different V_f profiles used in the sensitivity experiments (Figs. 11a–f). Figures 11a, 11c, and 11e display E for experiments with z_i = 9, 8, and 7 km, respectively, and $V_{f,1.2}$. Figures 11b, 11d, and 11f show E for the same z_i except for $V_{f,2.0}$. In general, sensitivity to particle reorganization and overall distribution placement was related to changes in particle positioning and particle residence time as controlled by z_i and the V_f profile. By decreasing z_i to 8 and 7 km with $V_{f,1.2}$ (Figs. 11b,c, respectively), the enhanced particle distribution extended further southeast compared to the control experiment. For example, near Binghamton, New York (red star in Figs. 11a,c,e), the southeast boundary of the particle distribution was approximately 50 km further southeast for z_i = 7 km (Fig. 11e) compared to z_i = 9 km (Fig. 11a). The same result was found for experiments with $V_{f,2.0}$ establishing that lower z_i results in a southeast shift in the location of the ice particle distribution. This can be attributed to a smaller particle fall depth within the deep southerly flow at higher altitudes.

For experiments comparing $V_{f,1.2}$ (Figs. 11a,c,e) with $V_{f,2.0}$ (Figs. 11b,d,f), magnitudes of E in the region of the greatest particle reorganization were slightly less for the $V_{f,2.0}$ experiments. For example, the magnitudes of E near the red star in Fig. 11a were 2.32–3.84, while in the same location in Fig. 11b, magnitudes of E were 2.12–3.08. Similar trends were found in the same location in the comparisons of Figs. 11c and 11d and Figs. 11e and 11f. Otherwise, E was nearly identical across the rest of the particle distributions in each comparison. This demonstrated that faster particle fall velocities resulted in slightly less particle reorganization by the horizontal flow as particles were subject to the flow for a shorter time similar to the results in Janiszeski et al. (2023).

Brought to you by University of Alabama in Huntsville | Unauthenticated | Downloaded 08/23/24 03:02 PM UTC

The results show that particles originating in the deep clouds of the comma head populated the north half of the precipitation band. A question naturally arises as to where the particles populating the southern half of the band originated. To examine this question, particles were released in the southern KMD from 4-km altitude, the approximate cloud-top altitude of clouds below the intruding dry slot air.

3) EXPERIMENTS IN THE SOUTHERN KMD

Figures 12a–f show the HRRR model RH overlaid with v_h for 7- to 2-km altitude at 1-km altitude intervals. The location of the heavier snowfall (2 km $Z_e > 20$ dBZ_e) is outlined in black and is beneath the southeast portion of the comma head. Figures 12a–c show the comma head and a pronounced dry slot extending from southwestern Pennsylvania eastward to the south of Long Island. Within the dry slot, no ice particles were present at or above 5-km altitude. The winds in the comma head region subjected ice particles originating at cloud top to a south to south-southwesterly flow of 20–35 m s^{-1} at 7 km that changed to south southeasterly and decreased slightly to 10–25 m s^{-1} by 3-km altitude above the heavy snowband. These winds transported ice particles northward initially and then north northwestward so that particles arrived on the north side of the heavy band at 2-km altitude as shown in the previous section. However, at 4-, 3-, and 2-km altitudes in Figs. 12d–f the northern side of the dry slot fills in with HRRR model RH values > 80% in a southerly to southeasterly flow of 30–40 m s^{-1}. This indicated that ice particles populating the south side of the heavy snowband were being transported at low levels by a strong, humid low-level flow at and below 4-km altitude from the southeast of the comma head region in the vicinity of northern New Jersey, northeastern Pennsylvania, Connecticut, and Rhode Island. This was quantitatively examined by releasing particles at 4-km altitude in the southern KMD (Fig. 13) using the control particle fall velocity profile ($V_{f,1.2}$) shown in Fig. 5d.

Within the 20-dBZ contour in Figs. 13a, 13c, and 13e, in the pink areas along the southern half of the band, the values of E ranged from 1.36 to 1.54 at 3 km, 1.36 to 1.68 at 2 km, and 1.44 to 2.08 at 1 km. The enhancements of E correspond closely to the axis of convergence with values between -20 and -40×10^{-5} s^{-1} at 3-km altitude. Along the same axis, the convergence was weaker, but still present, at lower altitudes, resulting in a continued increase in E to 2-km altitude. Simulations were also conducted using the $V_{f,2.0}$ fall velocity profile. Values of E were 0.04–0.12 less than the control run (not shown), a result of the particles having less time to reorganize.

The trajectories of the particles, projected into 2D planes, are shown in Figs. 14a and 14c. The locations of the 2D planes are shown in the inset of Fig. 14c. Along the westernmost plane, particles originating at 9 km across the comma head accumulated in the southern half of the northern KMD with a maximum E value of 3.61 located at the center of the band (denoted by the 20 dBZ contour in the inset map). Because the dry slot was impinging on the western edge of the southern KMD, no particles were released there although Figs. 14c and 14d show the fate of particles falling from beneath the dry slot clearly. Figures 14c and 14d show why it was necessary to overlap the domains, as particles originating at 9 km moved northwestward over 100 km during their fall to the 4-km level. In the eastern part of the band, particles from beneath the dry slot arrived on the southern side of the band with a maximum $E = 1.68$. These analyses show that the particles in the main band had two distinct sources: 1) on the northern side, from ice particles falling from the comma head, and 2) on the southern side, from particles originating at or below 4-km altitude beneath the dry slot region and transported by strong low-level flow off the Atlantic Ocean.

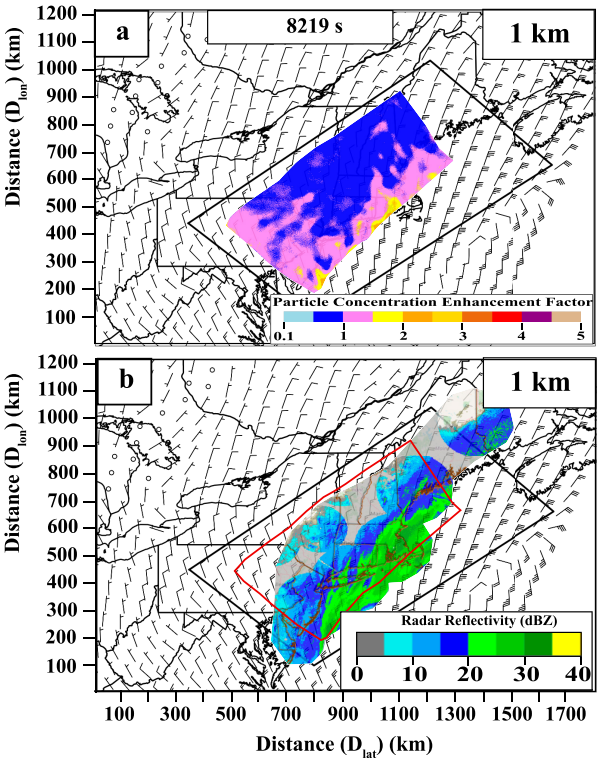

FIG. 16. (a) The 1-km altitude winds (long barb = 10 m s^{-1}) together with particle concentration enhancement factor E; (b) WSR-88D MRMS Z_e composite at 1 km with particle distribution outlined in red. The time since particle release is shown atop (a).

b. The 29–30 January storm analysis

1) THE CONTROL EXPERIMENT (NORTHERN PARTICLE RELEASE REGION)

Figures 15a–f show E in the context of v_h, including convergent and divergent flow, at 9-, 6-, and 4-km altitude for the control experiment of the 29–30 January 2022 storm. The control experiment had the same z_i and V_f profiles as the control experiment for the previous storm. The KMD for this storm is the domain within the black box in Fig. 3b. Positions (D_{lat}, D_{lon}) are referenced in kilometers with respect to the larger HRRR model grid with the origin at 36°N, 83°W (Fig. 15). The particle redistribution and E with depth can be explained by v_h, as the falling ice particles were transported northwestward

Brought to you by University of Alabama in Huntsville | Unauthenticated | Downloaded 08/23/24 03:02 PM UTC

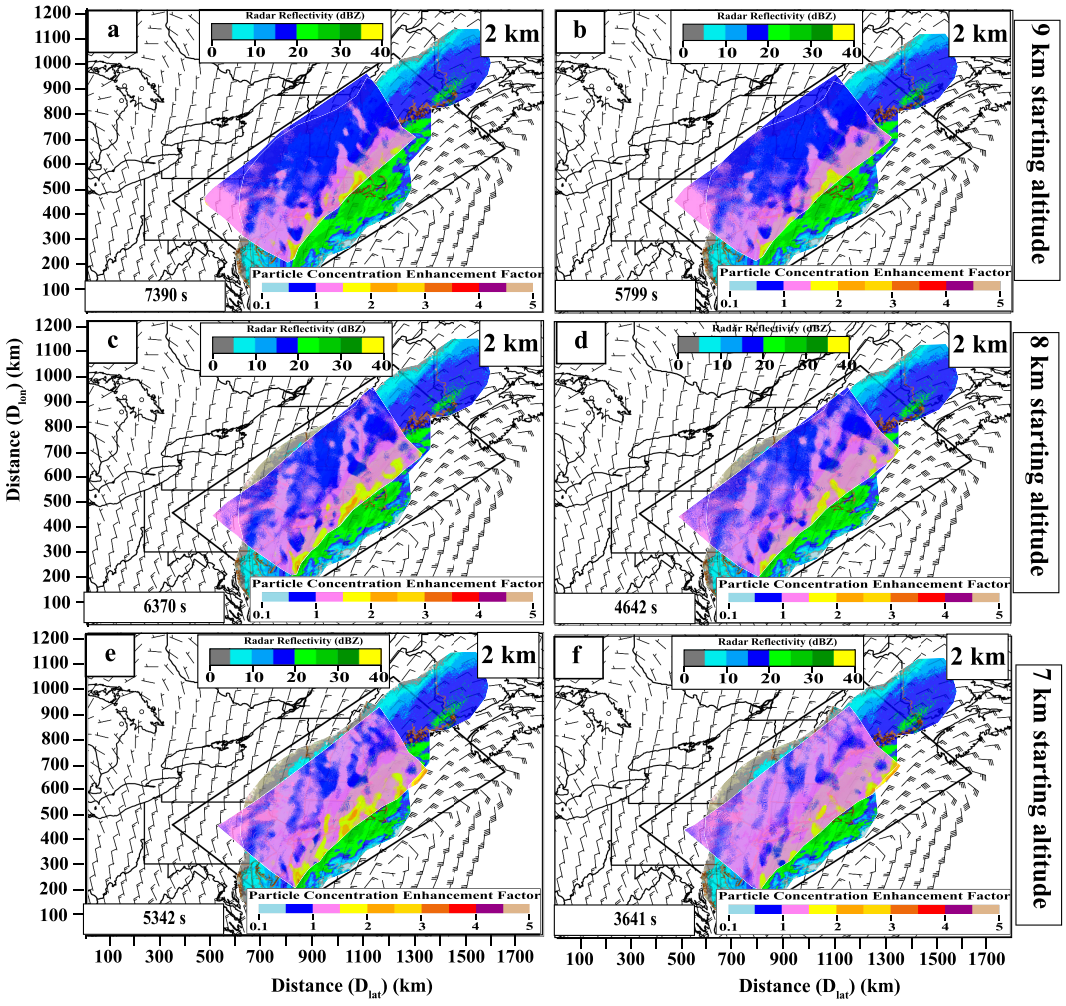

FIG. 17. As in Figs. 11a–f, but for the 29–30 Jan 2022 storm.

owing to a deep layer of south-southeasterly to southeasterly flow that decreased in magnitude with decreasing altitude from 40 to 50 m s^{-1} on the northeastern portion of the KMD at 9-km altitude (Fig. 15b) to 10–30 m s^{-1} in the same region at 4-km altitude (Fig. 15f). Over the southwestern portion of the KMD, the flow was southeasterly and somewhat weaker with 25–35-m s^{-1} flow at 9 km (Fig. 15b) decreasing to 5 m s^{-1} and becoming north-northwesterly at 4 km (Fig. 15f).

The flow was nearly nondivergent above 5-km altitude except for regions of divergence of 20–25 $\times$ 10^{-5} s^{-1} at 9-km altitude in a region bounded by approximately D_{lat} = 1000–1500 km and D_{lon} = 400–700 km (Fig. 15b). As a result, particles were transported northwestward, with values of E of 0.84–0.96 developing in the blue-shaded regions at 7- and 8-km altitude, signifying small particle concentration decreases, owing to areas of divergent flow (not shown). At 4-km altitude, v_h exhibited two weak regions of convergent flow within the KMD (Fig. 15f). The easternmost region was in the northeast portion of the KMD, slanting from southwest to northeast, between D_{lat} = 1000–1500 km and D_{lon} = 400–800 km with divergence values from −8 to −15 $\times$ 10^{-5} s^{-1}. A second, weaker, region of convergence arced through the center of KMD from D_{lat} = 1200 km and D_{lon} = 900 km at its northern edge to the southwestern corner of the KMD at approximately D_{lat} = 790 km and D_{lon} = 150 km. The easternmost region of convergent flow was collocated with the greatest E of 1.56–1.88 near D_{lat} = 1100 km and D_{lon} = 600 km (Fig. 15e). The southeastern portion of the particle distribution had small increases in the particle concentration with an E of 1.00–1.32 within the pink-shaded region (Fig. 15e). Further to the northwest, E of 0.88–0.96 was found in the blue-shaded region indicative of small particle concentration decreases (Fig. 15e).

The impact of the flows aloft on E at 1 km is shown in Fig. 16a. The maximum E was located at the southeast end of the particle distribution. The maximum E at the southeast edge of the particle distribution was 1.76–2.32 in a region approximately at D_{lat} = 1100 km and between D_{lon} = 400–500 km. The larger E at the southeast side of the particle distribution was collocated with the northern half of the main band (Fig. 16b). The southeast half of the band over the Atlantic

Brought to you by University of Alabama in Huntsville | Unauthenticated | Downloaded 08/23/24 03:02 PM UTC

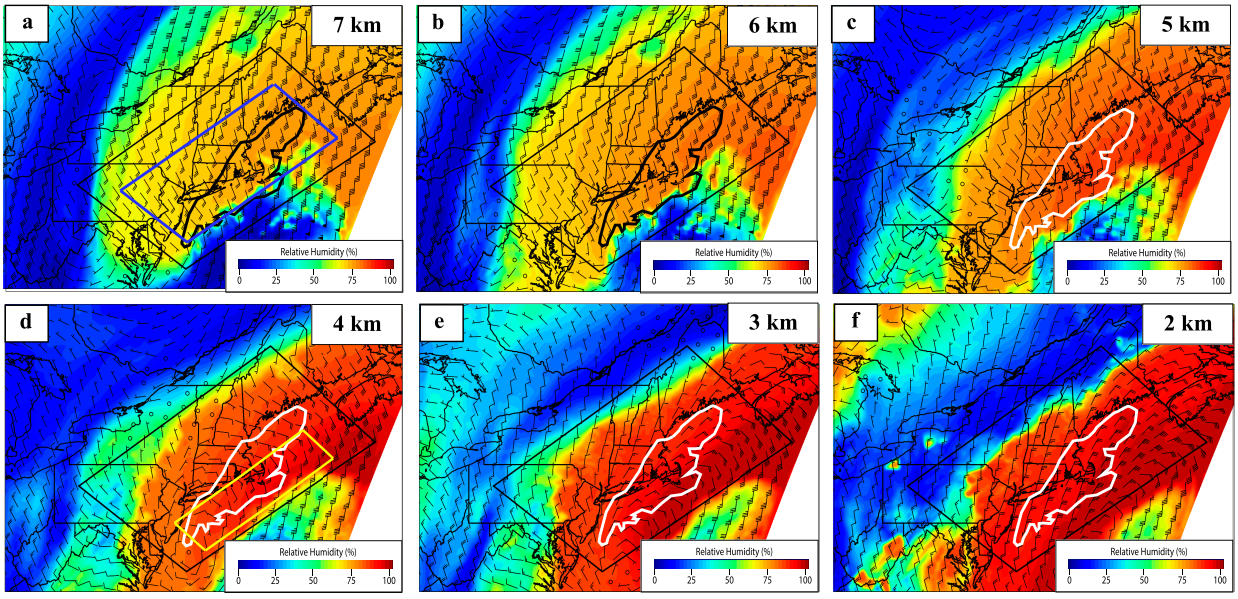

FIG. 18. As in Figs. 12a–f, but for the 29–30 Jan 2022 storm. The yellow box in (d) denotes the southern particle release region.

Ocean and near Cape Cod had no particles from the comma head (Fig. 16a).

2) SENSITIVITY STUDIES (NORTHERN PARTICLE RELEASE REGION)

Like the 16–17 December 2020 storm, the 2-km altitude MRMS reflectivity composite coverage of the main band was most complete and will be used in Figs. 17a–f to compare with the experiments showing sensitivity to z_i and V_f. As with the previous storm, sensitivity to changes in z_i was greater than sensitivity to changes in V_f. For example, the maximum E of 2.04 in Fig. 17a, which is from the control experiment, is found near $D_{\text{lat}} = 1100$ km and $D_{\text{lon}} = 500$ km, while in Fig. 17e, an experiment with $z_i = 7$ km and $V_{f,1.2}$, the maximum E is further southwest near $D_{\text{lat}} = 1050$ km and $D_{\text{lon}} = 450$ km with a slightly greater magnitude of 2.36. With lower z_i, the southeast edge of the particle distribution was further southeast compared to $z_i = 9$ km owing to particles residing for a shorter time in the southeasterly flow above 3-km altitude. For example, the southeastern edge of the distribution in Fig. 17e is approximately 50 km southeast of the southeastern edge of the distribution in Fig. 17a. For experiments comparing $V_{f,1.2}$ (Figs. 17a,c,e) with $V_{f,2.0}$ (Figs. 17b,d,f), magnitudes of E in the region of the greatest particle reorganization were slightly less for the $V_{f,2.0}$ experiments. The comparisons of V_f showed that with the $V_{f,2.0}$ profile, E magnitudes were 0.04–0.32 lower but were otherwise in the same general location, a result of the particles having less time to reorganize during their fall to the 2-km level.

The results show the ice particles falling from the comma head populated the northwest side of the main band for this storm. To determine the particle origin for the southeast side of the main band, the same analysis as Figs. 13a–f was done for the 29–30 January 2022 storm.

3) SOUTHERN PARTICLE RELEASE REGION

The location of 2 km $Z_e > 20$ dBZ_e is shown in either white or black in each panel in Fig. 18. A clear comma head shape is shown in the HRRR model RH fields in Figs. 18a–c over New Jersey, eastern New York, New England, and over the Atlantic Ocean near the East Coast, while a sharp dry slot is located southeast of this area further out over the Atlantic Ocean, south of Cape Cod, at 7, 6, and 5 km, respectively. Similar to the 16–17 December 2020 storm, the dry slot region begins to fill in with large increases in RH at and below 4 km especially near the southeastern boundary of the KMD. The flow at 4-, 3-, and 2-km altitude (Figs. 18d–f) is curved cyclonically from southeast to northeast over the Atlantic Ocean, transporting moist low-level air, denoted by RH values of greater than 80%, from low levels over the Atlantic Ocean toward the East Coast and subsequent main band. Particles were released at 4-km altitude within the yellow box in Fig. 18d to examine the contribution of particles from this region to the southern half of the primary band. The values of E in the southern half of the band ranged from 1.04 to 1.56 at 3 km and 1.24–2.16 at 2 km (Figs. 19a–c). The values of E at 1 km were similar to 2 km (Fig. 19e). As with the 16–17 December 2020 storm, simulations conducted with the $V_{f,2.0}$ particle fall velocity profile exhibited only a small decrease in the values of E because of the shorter time to fall to 2 km. A long axis of convergent flow along the coastline at 3 km from -5 to -15×10^{-5} s^{-1} contributed to the concentration enhancement.

The trajectories of the particles projected into a 2D plane and the enhancement factor are shown in Figs. 20a and 20b. The location of the plane is shown in the inset in Fig. 20a. As with the previous case, particles were transported to the northwest by the upper-level flow in the comma head region toward the northwest side of the band, while the low-level flow was the source of ice particles on the southeast side of

Brought to you by University of Alabama in Huntsville | Unauthenticated | Downloaded 08/23/24 03:02 PM UTC

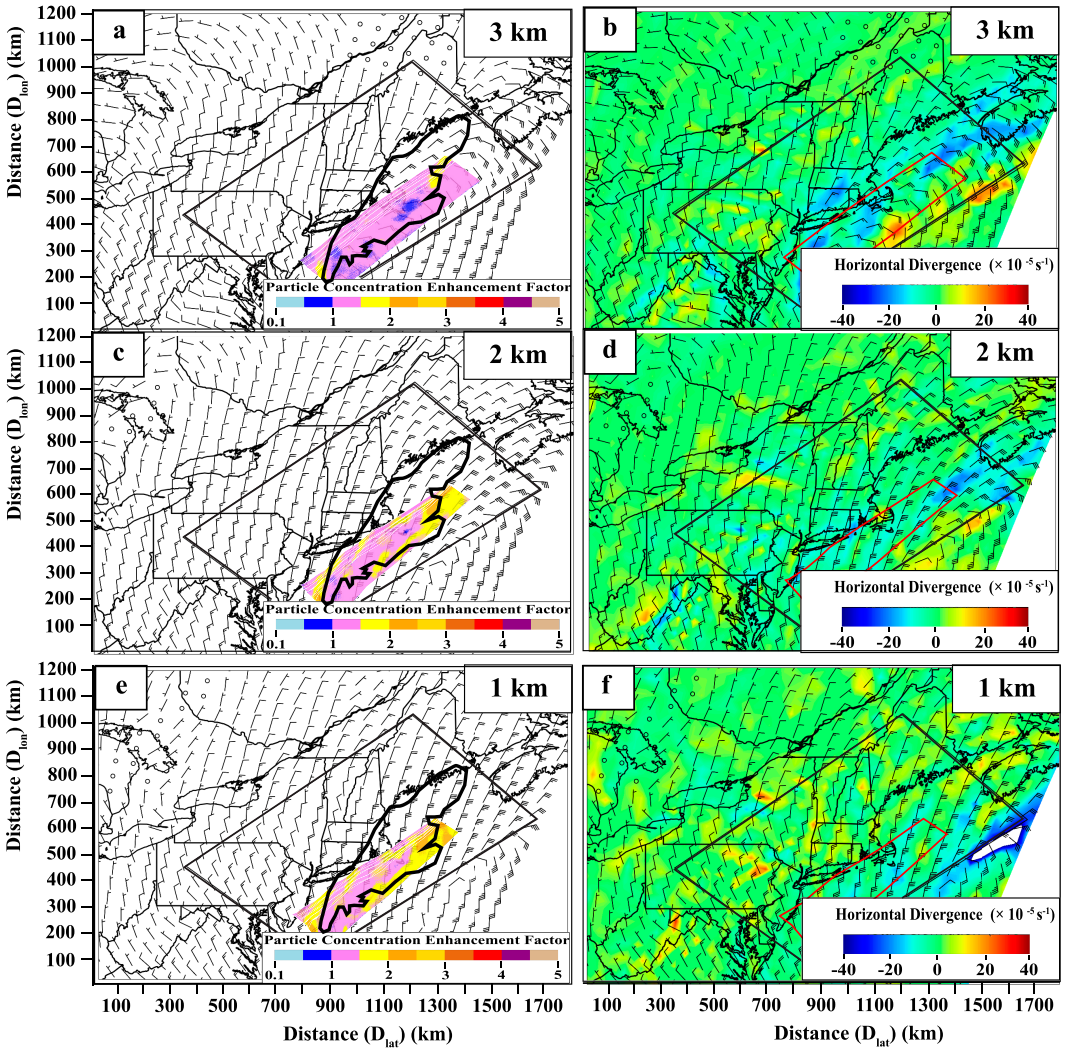

FIG. 19. As in Fig. 13, but for the southeast particle release region of the 29–30 Jan 2022 storm.

the band. Similar to the 16–17 December 2020 storm, this analysis shows that the particles in the main band had two distinct sources: 1) on the northwestern side, from ice particles falling from the comma head, and 2) on the southeastern side, from particles falling from clouds at or below 4-km altitude beneath the cyclone dry slot and transported northwestward by a strong low-level flow off the Atlantic Ocean.

5. Discussion

Forecasting the location of heavy snowfall, typically organized in precipitation bands, requires an understanding of where snowbands are most likely to occur and what processes contribute to their formation. In this paper, experiments were conducted to isolate the role of three-dimensional horizontal kinematic flow in reorganizing ice particles falling from the upper part of the comma head and from low-level clouds beneath the storms' upper-tropospheric dry slot in two northeast U.S. winter storms where a distinct major low-level snowband was present. As noted in the introduction, one factor leading to the development of such bands is kinematic flow rearranging ice particles beneath cloud top into linear banded features near the surface (Janiszeski et al. 2023). These experiments investigated this factor by arranging particles uniformly spaced at cloud-top altitudes, based on HRRR model relative humidity and local sounding analyses, and letting particles fall at velocities characteristic of such storms within the full three-dimensional horizontal kinematic flow until they reached 1-km altitude. Particle concentrations were then compared to WSR-88D reflectivity at 3, 2, and 1 km to determine whether particles were reorganized consistent with low-level bands and were consistent with regions of convergence or divergence and frontogenesis.

The results from the 16–17 December 2020 and 29–30 January 2022 storms, including both particle fall velocity profiles and all initial particle release altitudes, found that ice particles falling through the comma head starting from either 9-, 8-, or 7-km

Brought to you by University of Alabama in Huntsville | Unauthenticated | Downloaded 08/23/24 03:02 PM UTC

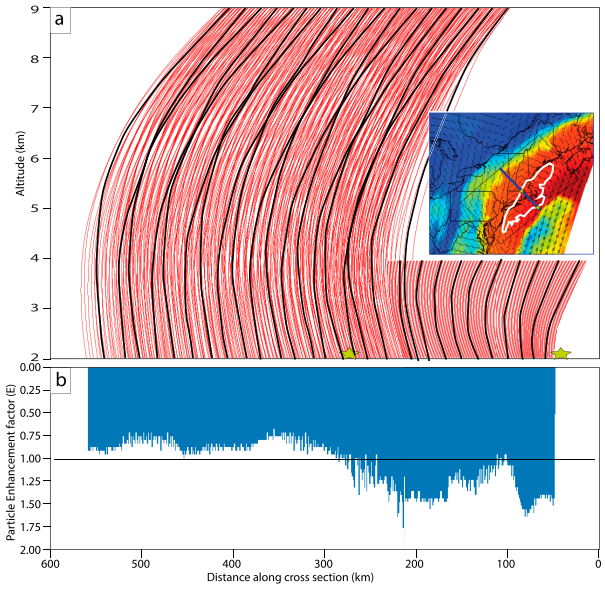

FIG. 20. (a) Red, full set of 2D trajectories of particles originating in the northern and southern particle release regions. Particles descend from 9 km in the northern particle release region and 4 km in the southern particle release region in the cross-sectional plane along the blue line in the inset in (a). Black lines show the select trajectories. The stars denote the boundaries of the 20-dBZ contour in the inset. (b) Histogram of the particle enhancement factor E corresponding to the trajectories in (a). Inset: RH and wind at 4 km with the KMD shown. The blue line corresponds to the cross section in (a).

altitude, were transported to the north or northwest by a 4–5-km-deep southeasterly, south-southeasterly, or southerly flow with higher concentrations arriving on the north or northwest half of the main observed low-level snowbands. Particle concentrations in those locations were increased by convergent horizontal flow with the greatest particle concentration enhancement factors E of 2.32–3.84 for the 16–17 December 2020 storm and 1.76–2.32 for the 29–30 January 2022 storm, respectively, collocated with the highest observed reflectivity in each band. However, no ice particles from the comma head arrived within the south or southeastern half of the main bands. Low-level HRRR model relative humidity and horizontal flows beneath the upper-tropospheric dry slot suggested that the source of snowfall in those regions was not from comma head but rather from particle transport by moist low-level flows off the Atlantic Ocean interacting with low-level fronts in each storm. Experiments were conducted releasing particles at 4-km altitude beneath the upper-tropospheric dry slot regions of each storm to determine whether these particles populated the southern half of the band. Particle enhancements in the southern half of the band from particles in this region ranged from $E = 1.36$–2.08 and $E = 1.04$–2.16 for the 16–17 December 2020 and 29–30 January 2022 storms, respectively. These experiments indicated that for the heavy banded snowfall in both storms, the snowfall had two source regions: 1) on the north or northwestern side, from ice particles falling from the comma head, and 2) on the southeastern side, for particles falling from clouds at or below 4-km altitude and transported northwestward by strong low-level flows off the Atlantic Ocean.

The analysis and findings of this research are consistent with the previous investigations of midlatitude winter storm cloud and precipitation structures described in Rosenow et al. (2014), Rauber et al. (2014), and Varcie et al. (2023) where airborne radar observations of clouds and precipitation show two distinct regions within such storms. Figures 21a and 21b show a comparison of observed equivalent radar reflectivity structures from Rosenow et al. (2014) (Fig. 21a) with observations of a midlatitude cyclone on 2 February 2015 along the East Coast from Rauber et al. (2017) (Fig. 21b), both from airborne W-band cloud radars. On the north side of the storms, an 8–10-km deep stratiform cloud, referred to as the stratiform region, is observed, with cloud-top generating cells atop the storm and precipitation fallstreaks beneath. Further to the south, lower-level clouds and elevated convection, referred to as the convective region, are observed with cloud tops between 4- and 6-km altitude. As shown in the HRRR model RH and v_h analyses of the 16–17 December 2020 and 29–30 January 2022 storms (see Figs. 12a–f and 18a–f), deep stratiform clouds were located to the northwest of the 900-hPa geopotential low with cloud tops of 9 km, while southeast of the comma head, cloud tops were near 4-km altitude with more convective structured precipitation. The main bands in each storm were due to ice particles arriving from both the stratiform and convective regions at altitudes where they were observable by surveillance radars. This suggests that the findings in this paper are consistent with snowfall reorganization typical of midlatitude winter cyclones.

6. Conclusions

This paper focused on ice particle reorganization beneath cloud top within the comma head region of two major U.S. East Coast winter storms by kinematic flows, and the effect of particle reorganization on the ice particle concentrations within observed primary low-level snowbands. The kinematic flows were taken from the initialization of the HRRR model winds at times when these snowbands were intense. Initial particle placement was based on HRRR model RH and observed sounding analyses from each storm, and particle fall velocities were based on past airborne radar vertical radial velocity measurements from the IMPACTS and PLOWS field campaigns and microphysical observations of snowfall from Griffin et al. (2014), Picca et al. (2014), and Ganetis and Colle (2015). The key findings of this paper are as follows:

1) For both storms, ice particles falling through the comma head starting from either 9-, 8-, or 7-km altitude, were transported to the north or northwest by a 4–5-km-deep southeasterly, south-southeasterly, or southerly flow with higher concentrations arriving on the north or northwest half of the primary observed low-level snowband in each case.
2) Particle concentrations, collocated with the highest observed reflectivity in each band, were increased by convergent horizontal flow, with the greatest particle concentration

Brought to you by University of Alabama in Huntsville | Unauthenticated | Downloaded 08/23/24 03:02 PM UTC

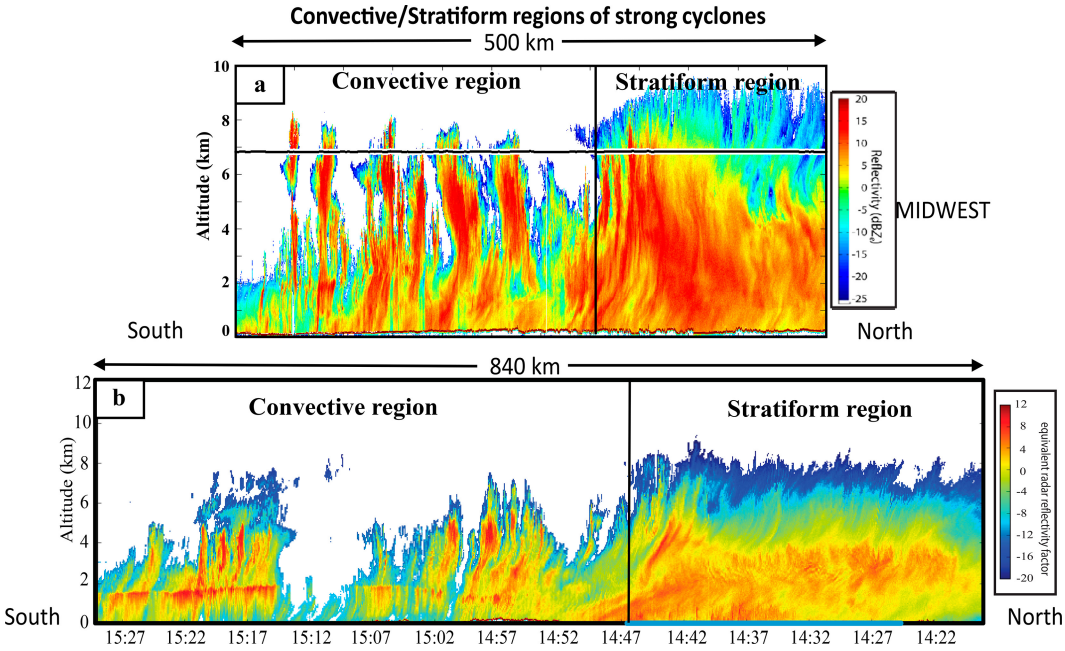

FIG. 21. (a) Observed equivalent radar reflectivity factor from the Wyoming Cloud Radar (WCR) aboard the National Science Foundation/National Center for Atmospheric Research (NSF/NCAR) C-130 aircraft (from Rosenow et al. 2014, their Fig. 6a); (b) observed equivalent radar reflectivity factor from the HIAPER Cloud Radar aboard the NSF/NCAR Gulfstream-V aircraft from 1418 to 1531 UTC 2 Feb 2015. The convective and stratiform regions of each storm are labeled, respectively.

enhancement E of 2.32–3.84 for the 16–17 December 2020 storm and 1.76–2.32 for the 29–30 January 2022 storm, respectively.

3) Sensitivity studies showed that shorter particle residence time (lower initial particle release altitude and/or faster particle fall velocity) resulted in reduced particle reorganization into the bands, consistent with the findings of Janiszeski et al. (2023).
4) Experiments releasing particles from 4-km altitude associated with clouds beneath the cyclones' dry slot showed that the source of snowfall in the southern or southeastern part of each band was not from comma head but rather from particle transport by moist low-level flows off the Atlantic Ocean interacting with convergence associated with low-level fronts in each storm. The particle concentration enhancements in the southern part of the bands ranged from 1.36 to 2.08 for the 16–17 December 2020 and 1.04–2.16 and 29–30 January 2022 storms.
5) From a simplified kinematic viewpoint in these experiments, the heavy banded snowfall in both storms had two source regions: 1) on the north or northwestern side, from ice particles falling from the comma head, and 2) on the southeastern side, from particles falling at or below 4-km altitude beneath the upper-tropospheric dry slot.
6) Based on previous airborne radar observations of winter storm cloud and precipitation structures, this snowfall reorganization is consistent with structures observed with airborne radar in storms along the U.S. East Coast and central United States.

This paper examined the hypothesis that ice particle concentrations can be enhanced within precipitation bands as a result of reorganization of particles by kinematic flows. While the findings support this hypothesis and give information on the source of particles in the bands, they do not definitively determine the cause of precipitation banding. Other factors such as snow growth as a result of large-scale ascent in an elongated updraft in the secondary circulation associated with frontogenesis, snow growth due to ascent in convection from the release of mesoscale instabilities within the updraft associated with frontogenesis, and the general effect of vertical motions on snow particle trajectories (Lackmann and Thompson 2019) must be considered for a full understanding of snowband formation. This work shows, however, that kinematics alone contributes to snowband formation by concentrating ice particles into regions consistent with snowband locations in winter storms.

Acknowledgments. This work was funded by the NASA Earth Venture Suborbital-3 (EVS-3) program under Grant 80NSSC19K0355 (UIUC).

Data availability statement. Profiling of Winter Storms (PLOWS) W-band Wyoming Cloud Radar data used to construct Fig. 8 are available at https://data.eol.ucar.edu/master_lists/generated/plows/. IMPACTS W-band CRS data used to construct Fig. 7 are available from the NASA EOSDIS Global Hydrology Resource Center Distributed Active Archive Center, Huntsville, Alabama, U.S.A., at https://doi.org/10.5067/IMPACTS/

Brought to you by University of Alabama in Huntsville | Unauthenticated | Downloaded 08/23/24 03:02 PM UTC

DATA101. The HRRR model data are archived by the University of Utah and are available at https://home.chpc.utah.edu/~u0553130/Brian_Blaylock/cgi-bin/hrrr_download.cgi (last accessed March 2023).

REFERENCES

Carbone, R. E., and A. R. Bohne, 1975: Cellular snow generation—A Doppler radar study. *J. Atmos. Sci.*, **32**, 1384–1394, https://doi.org/10.1175/1520-0469(1975)032<1384:CSGDRS>2.0.CO;2.

Douglas, R. H., K. L. S. Gunn, and J. S. Marshall, 1957: Pattern in the vertical of snow generation. *J. Meteor.*, **14**, 95–114, https://doi.org/10.1175/1520-0469(1957)014<0095:PITVOS>2.0.CO;2.

Draxler, R. R., and G. D. Hess, 1998: An overview of the HYSPLIT_4 modelling system for trajectories, dispersion, and deposition. *Aust. Meteor. Mag.*, **47**, 295–308.

Ganetis, S. A., and B. A. Colle, 2015: The thermodynamic and microphysical evolution of an intense snowband during the northeast U.S. blizzard of 8–9 February 2013. *Mon. Wea. Rev.*, **143**, 4104–4125, https://doi.org/10.1175/MWR-D-14-00407.1.

Ganetis, S., B. A. Colle, S. E. Yuter, and N. P. Hoban, 2018: Environmental conditions associated with observed snowband structures within northeast U.S. winter storms. *Mon. Wea. Rev.*, **146**, 3675–3690, https://doi.org/10.1175/MWR-D-18-0054.1.

Griffin, E. M., T. J. Schuur, A. V. Ryzhkov, H. D. Reeves, and J. C. Picca, 2014: A polarimetric and microphysical investigation of the northeast blizzard of 8–9 February 2013. *Wea. Forecasting*, **29**, 1271–1294, https://doi.org/10.1175/WAF-D-14-00056.1.

Gunn, K. L. S., M. P. Langleben, A. S. Dennis, and B. A. Power, 1954: Radar evidence of a generating level for snow. *J. Meteor.*, **11**, 20–26, https://doi.org/10.1175/1520-0469(1954)011<0020:REOAGL>2.0.CO;2.

Hobbs, P. V., and J. D. Locatelli, 1978: Rainbands, precipitation cores, and generating cells in a cyclonic storm. *J. Atmos. Sci.*, **35**, 230–241, https://doi.org/10.1175/1520-0469(1978)035<0230:RPCAGC>2.0.CO;2.

Janiszeski, A., R. M. Rauber, B. F. Jewett, G. M. McFarquhar, T. J. Zaremba, and J. E. Yorks, 2023: A kinematic modeling study of the re-organization of snowfall between cloud-top generating cells and low-level snow bands in midlatitude winter storms. *J. Atmos. Sci.*, **80**, 2729–2745, https://doi.org/10.1175/JAS-D-23-0024.1.

Keeler, J. M., R. M. Rauber, B. F. Jewett, G. M. McFarquhar, R. M. Rasmussen, L. Xue, C. Liu, and G. Thompson, 2017: Dynamics of cloud-top generating cells in winter cyclones. Part III: Shear and convective organization. *J. Atmos. Sci.*, **74**, 2879–2897, https://doi.org/10.1175/JAS-D-16-0314.1.

Kocin, P. J., and L. W. Uccellini, 2005: *Northeast Snowstorms*, Vols. 1 and 2, *Meteor. Monogr.*, No. 54, Amer. Meteor. Soc., 818 pp.

Kumjian, M. R., and K. A. Lombardo, 2017: Insights into the evolving microphysical and kinematic structure of northeastern U.S. winter storms from dual-polarization Doppler radar. *Mon. Wea. Rev.*, **145**, 1033–1061, https://doi.org/10.1175/MWR-D-15-0451.1.

——, S. A. Rutledge, R. M. Rasmussen, P. C. Kennedy, and M. Dixon, 2014: High-resolution polarimetric radar observations of snow-generating cells. *J. Appl. Meteor. Climatol.*, **53**, 1636–1658, https://doi.org/10.1175/JAMC-D-13-0312.1.

Lackmann, G. M., and G. Thompson, 2019: Hydrometeor lofting and mesoscale snowbands. *Mon. Wea. Rev.*, **147**, 3879–3899, https://doi.org/10.1175/MWR-D-19-0036.1.

Leonardo, N. M., and B. A. Colle, 2024: Analysis of snow multibands and their environments with high-resolution idealized simulations. *Mon. Wea. Rev.*, **152**, 925–943, https://doi.org/10.1175/MWR-D-23-0211.1.

Locatelli, J. D., and P. V. Hobbs, 1974: Fall speeds and masses of solid precipitation particles. *J. Geophys. Res.*, **79**, 2185–2197, https://doi.org/10.1029/JC079i015p02185.

Marshall, J. S., 1953: Precipitation trajectories and patterns. *J. Meteor.*, **10**, 25–29, https://doi.org/10.1175/1520-0469(1953)010%3C0025:PTAP%3E2.0.CO;2.

McFarquhar, G. M., and Coauthors, 2011: Indirect and Semi-Direct Aerosol Campaign (ISDAC): The impact of Arctic aerosols on clouds. *Bull. Amer. Meteor. Soc.*, **92**, 183–201, https://doi.org/10.1175/2010BAMS2935.1.

McMurdie, L. A., and Coauthors, 2022: Chasing snowstorms: The Investigation of Microphysics and Precipitation for Atlantic Coast-Threatening Snowstorms (IMPACTS) campaign. *Bull. Amer. Meteor. Soc.*, **103**, E1243–E1269, https://doi.org/10.1175/BAMS-D-20-0246.1.

Nicosia, D. J., and R. H. Grumm, 1999: Mesoscale band formation in three major northeastern United States snowstorms. *Wea. Forecasting*, **14**, 346–368, https://doi.org/10.1175/1520-0434(1999)014<0346:MBFITM>2.0.CO;2.

NOHRSC, 2023: National gridded snowfall analysis. National Weather Service Office of Water Prediction, accessed 4 March 2023, https://www.nohrsc.noaa.gov/snowfall/.

Novak, D. R., L. F. Bosart, D. Keyser, and J. S. Waldstreicher, 2004: An observational study of cold season-banded precipitation in northeast U.S. cyclones. *Wea. Forecasting*, **19**, 993–1010, https://doi.org/10.1175/815.1.

——, B. A. Colle, and R. McTaggart-Cowan, 2009: The role of moist processes in the formation and evolution of mesoscale snowbands within the comma head of northeast U.S. cyclones. *Mon. Wea. Rev.*, **137**, 2662–2686, https://doi.org/10.1175/2009MWR2874.1.

——, ——, and A. R. Aiyyer, 2010: Evolution of mesoscale precipitation band environments within the comma head of northeast U.S. cyclones. *Mon. Wea. Rev.*, **138**, 2354–2374, https://doi.org/10.1175/2010MWR3219.1.

Picca, J. C., D. M. Schultz, B. A. Colle, S. Ganetis, D. R. Novak, and M. J. Sienkiewicz, 2014: The value of dual-polarization radar in diagnosing the complex microphysical evolution of an intense snowband. *Bull. Amer. Meteor. Soc.*, **95**, 1825–1834, https://doi.org/10.1175/BAMS-D-13-00258.1.

Plummer, D. M., G. M. McFarquhar, R. M. Rauber, B. F. Jewett, and D. C. Leon, 2014: Structure and statistical analysis of the microphysical properties of generating cells in the comma head region of continental winter cyclones. *J. Atmos. Sci.*, **71**, 4181–4203, https://doi.org/10.1175/JAS-D-14-0100.1.

——, ——, ——, ——, and ——, 2015: Microphysical properties of convectively generated fall streaks within the stratiform comma head region of continental winter cyclones. *J. Atmos. Sci.*, **72**, 2465–2483, https://doi.org/10.1175/JAS-D-14-0354.1.

Rauber, R. M., and Coauthors, 2014: Stability and charging characteristics of the comma head region of continental winter cyclones. *J. Atmos. Sci.*, **71**, 1559–1582, https://doi.org/10.1175/JAS-D-13-0253.1.

Brought to you by University of Alabama in Huntsville | Unauthenticated | Downloaded 08/23/24 03:02 PM UTC

——, S. M. Ellis, J. Vivekanandan, J. Stith, W.-C. Lee, G. M. McFarquahar, B. F. Jewett, and A. Janiszeski, 2017: Fine-scale structure of a snowstorm over the northeastern United States: A first look at high-resolution HIAPER cloud radar observations. *Bull. Amer. Meteor. Soc.*, **98**, 253–269, https://doi.org/10.1175/BAMS-D-15-00180.1.

Rosenow, A. A., D. M. Plummer, R. M. Rauber, G. M. McFarquhar, B. F. Jewett, and D. Leon, 2014: Vertical velocity and physical structure of generating cells and convection in the comma head region of continental winter cyclones. *J. Atmos. Sci.*, **71**, 1538–1558, https://doi.org/10.1175/JAS-D-13-0249.1.

Schultz, D. M., and J. A. Knox, 2007: Banded convection caused by frontogenesis in a conditionally, symmetrically, and inertially unstable environment. *Mon. Wea. Rev.*, **135**, 2095–2110, https://doi.org/10.1175/MWR3400.1.

Smith, T. M., and Coauthors, 2016: Multi-Radar Multi-Sensor (MRMS) severe weather and aviation products: Initial operating capabilities. *Bull. Amer. Meteor. Soc.*, **97**, 1617–1630, https://doi.org/10.1175/BAMS-D-14-00173.1.

Stark, D., B. A. Colle, and S. E. Yuter, 2013: Observed microphysical evolution for two East Coast winter storms and the associated snow bands. *Mon. Wea. Rev.*, **141**, 2037–2057, https://doi.org/10.1175/MWR-D-12-00276.1.

Syrett, W. J., B. A. Albrecht, and E. E. Clothiaux, 1995: Vertical cloud structure in a midlatitude cyclone from a 94-GHz radar. *Mon. Wea. Rev.*, **123**, 3393–3407, https://doi.org/10.1175/1520-0493(1995)123<3393:VCSIAM>2.0.CO;2.

Varcie, M. M., and Coauthors, 2023: Precipitation growth processes in the comma-head region of the 7 February 2020 northeast snowstorm: Results from IMPACTS. *J. Atmos. Sci.*, **80**, 3–29, https://doi.org/10.1175/JAS-D-22-0118.1.

Wexler, R., 1955: Radar analysis of precipitation streamers observed 25 February 1954. *J. Meteor.*, **12**, 391–393, https://doi.org/10.1175/1520-0469(1955)012<0391:RAOPSO>2.0.CO;2.

——, and D. Atlas, 1959: Precipitation generating cells. *J. Meteor.*, **16**, 327–332, https://doi.org/10.1175/1520-0469(1959)016<0327:PGC>2.0.CO;2.

Brought to you by University of Alabama in Huntsville | Unauthenticated | Downloaded 08/23/24 03:02 PM UTC